Indian Journal of Chemistry
Vol. 62, May 2023, pp. 472-497
DOI: 10.56042/ijc.v62i5.1426

Design and development of salen-type Schiff bases as potential antivirus agents: Experimental and theoretical approach

Sunil Kumar & Mukesh Choudhary*
Department of Chemistry, National Institute of Technology Patna, Patna 800 005, Bihar, India
*E-mail: mukesh@nitp.ac.in

Received 21 August 2022; accepted (revised) 24 April 2023

Five new salen-type Schiff base compounds (**LH_2-L^4H_2**) have been designed and synthesized and their interaction with SARS-CoV-2, HIV virus and DNA polymerase IV have been studied by *in silico* approaches. The newly synthesized salen-type Schiff base ligands have been derived from the condensation of substituted salicylaldehydes and ethylenediamine in MeOH. ^1H and ^{13}C NMR, FT-IR and UV-Vis spectral techniques have been applied in order to confirm the structural elucidation of the desired products. The crystal structure of the compound **LH_2** is determined by the single crystal X-ray diffraction. Density functional theory (DFT) calculations have been employed to evaluate the optimized electronic structure, HOMO-LUMO, energy gap, and global parameters. Extensive classical molecular dynamics simulations have been performed to investigate the consequences of docking of the synthesized ligand, LH_2 on a protein moiety (PDB id: 7O46). Molecular docking studies have been performed on compounds (**LH_2-L^4H_2**) to predict the binding mode and interactions between the ligands and the main protease of the SARS-CoV-2 (PDB ID: 7O46) for COVID-19 and HIV virus (PDB ID: 1UUI). The molecular docking results show that compounds (**LH_2-L^4H_2**) with SARS-CoV-2 and HIV virus exhibit good binding affinity at binding site of receptor protein. As potential drug candidates, Swiss-ADME and target predictions (pharmacokinetics and drug-likeness prediction) analyses have also been studied and the results are compared with Chloroquine (CQ) and Hydroxychloroquine (HCQ) as anti-SARS-CoV-2 drugs. Salen-type ligands have also been docked into the DNA polymerase IV (PDB ID: 5YUX) for surface binding and intercalation. Overall, the present study offers the therapeutic potential for a series of compounds (**LH_2-L^4H_2**) for biomedical applications with reference to coronavirus (SARS-CoV-2) and HIV virus.

Keywords: Salen-type compounds, SARS-CoV-2, HIV virus, DNA polymerase, Molecular docking

Salen-type Schiff base compounds are well-known for its ease of preparation, condensation of primary ammines with ketones or aldehydes under specific conditions resulted in the formation of azomethine group containing compounds[1,2]. They are particularly polynuclear ligands, consisting of two imino nitrogen and two phenolic oxygen donors, are stable due to their chelating effect and are used as homogeneous and heterogeneous catalysts in various organic conversion reactions[3-6]. Given their crucial application in catalysis, their synthetic flexibility, rich in coordination, resulted in various field of applications including clinical, biomedical, analytical and biological properties with reference to SARS-CoV-2 and HIV virus[7-9]. Besides this, recently the world is in quest for effective drug to treat SARC-CoV-2. One target that has received much attention is the SARS (severe acute respiratory syndrome) CoV-2 main protease (M^{pro}). SARS-CoV-2 is a highly infectious virus that causes COVID-19, a homodimer whose structure has been determined[10-12]. SARS-CoV-2 causes infected cells to express a main protease (M^{pro}) that is responsible for site-specifically cleaving the polyprotein, which is translated from viral m-RNA within human cells[13]. The nucleosides usually show antiviral activity by inhibiting viral replication through the backbone of cellular division, impairment of DNA/RNA synthesis or inhibition of cellular or viral enzyme activity as well as inhibition of SARS-CoV-2 replication and infection. The essential role of SARS-CoV-2 M^{pro}, as well as the success of HIV protease inhibitors in the treatment of HIV/AIDS, makes M^{pro} an attractive therapeutic target to treat SARS-CoV-2[14]. Several different antiviral agents, including re-purposed drugs, are under testing in clinical trials to assess their efficacy against the new virus, but the quest for an effective treatment against COVID-19 is still open[15-17]. Considering the above facts, herein, five newsalen-type Schiff bases (**LH_2-L^4H_2**) have been designed and synthesized as potential antivirus drug candidates. In this work, we prepare new compounds (**LH_2-L^4H_2**) to elaborate their structures and antivirus properties with reference to coronavirus (SARS-CoV-2) and HIV virus. Five new compounds (**LH_2-L^4H_2**) were synthesized using ethylene diamine and related aldehydes (5-Bromosalicylaldehyde, 3,5-Dichlorosalicylaldehyde, 5-Bromo-3-methoxy-2-hydroxy-benzaldehyde, 3,5-Diiodosalicylaldehyde, 3,5-Dinitrosalicylaldehyde). They were fully characterized by different spectroscopic and physicochemical methods and DFT based computational approaches. Molecular docking studies were performed on compounds (**LH_2-L^4H_2**) to predict the binding mode and interactions between the ligands and the main protease of the SARS-CoV-2 (PDB ID: 7O46) for COVID-19 and HIV virus (PDB ID: 1UUI). Salen-type ligands were alsodocked into the DNA polymerase IV (PDB ID: 5YUX) for surface binding and intercalation. The main goal of our in-silico molecular docking is to identify antivirus potential of thecompounds (**LH_2-L^4H_2**) against coronavirus and HIV virus which can inhibit main protease of the SARS-CoV-2 and HIV effectively. Further study is indeed required to validate its action on SARS-CoV-2 and HIV virus. The molecular docking results showed that the compounds (**LH_2-L^4H_2**) with coronavirus (SARS-CoV-2) and HIV virus exhibited good binding affinity at binding site of receptor protein. Swiss-ADME and target predictions (pharmacokinetics and drug-likeness prediction) analyses are also studied and the results are compared with Chloroquine (CQ) and Hydroxychloroquine (HCQ) as anti-SARS-CoV-2 drugs. Overall, the present study will be used for the therapeutic potential of a series of new compounds (**LH_2-L^4H_2)** for biomedical applications with reference to the coronavirus (SARS-CoV-2) and HIV virus.

Results and Discussion

Synthesis and characterization

Five new compounds (**LH_2-L^4H_2**) were synthesized by condensing substituted salicylaldehydes (5-Bromosalicylaldehyde, 3,5-Dichlorosalicylaldehyde, 5-Bromo-3-methoxy-2-hydroxy-benzaldehyde, 3,5-Diiodosalicylaldehyde, 3,5-Dinitrosalicylaldehyde) with ethylene diamine in molar ratio 2:1 in EtOH solution (Scheme 1). They are stable in solid state, soluble in water and other common organic solvents.They were characterized by different spectroscopic and quantum computational approaches. The crystal structure of the compound **LH_2** is determined by the single crystal X-ray diffraction. The crystal was isolated from the mother liquor and the crystal quality of the **LH_2** is observed under a polarizing microscope for the X-ray diffraction studies. The absorption coefficient μ of this material is 5.156 mm^{-1} at this wavelength (λ = 0.71073Å) and the minimum and maximum transmissions are 0.745 and 0.382. The crystallographic data along with structure refinement parameters, including CCDC Nos is given in the Table 1. Selected bond lengths and bond angles are listed in the Table S1. Table S2 show hydrogen bonds for salen-type compounds. Fig. 1 shows the ORTEP view of the compound **LH_2** with 50% thermal ellipsoid and with atom labelling while unit cell packing diagram was given in Fig. 2. Hydrogen atoms are omitted for clarity. Crystal Data: $C_{16}H_{14}Br_2N_2O_2$,

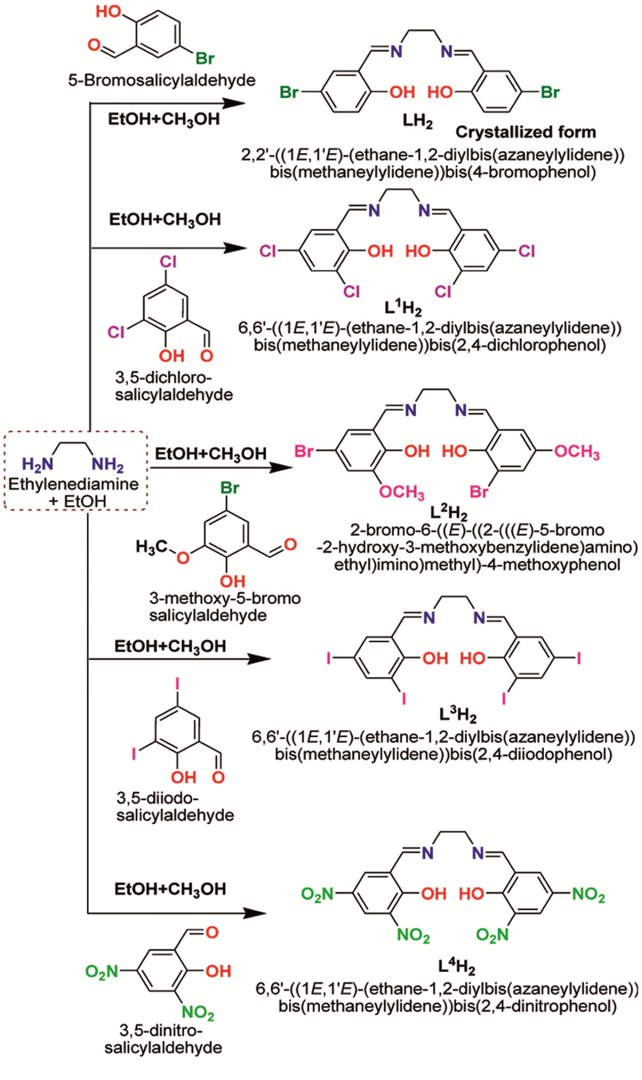

Scheme 1 — Synthetic routes leading of salen-type compounds (**LH_2-L^4H_2**)

Mr = 426.09, crystal system= Monoclinic, space group = *P2₁/c,*unit cell: a = 18.092(4) Å, b = 7.1364(13) Å, c = 6.1092(11) Å, $\alpha = \gamma = 90°$, $\beta = 93.514(5)$, $V = 787.3(3)$ Å^3, $T = 220(2)$ K, $Z = 2$, $Z' = 0.5$, μ(Mo Kα) = 0.71073 Å, μ= 5.156 mm^{-1}, F(000)= 420, 26375 collected reflections measured, 1972 unique ($R_{int} = 0.1086$) which were used in all calculations. The final $wR_2$was 0.1979 (all data) (I≥2 σ (I)) was measured. The structure was refined anisotropic ally on F^2. An H atom was refined isotropic ally. No crystal decay was observed. Additionally inspiring from recent developments to find an inhibitors of the SARS-CoV-2 main protease and HIV virus, in-silico molecular docking studies were performed on the salen-type Schiff bases (**LH_2-L^4H_2**) to predict the binding mode and interactions between the ligands and the main protease of the SARS-CoV-2 (PDB ID: 7O46) for COVID-19 and HIV virus (PDB ID: 1UUI). The X-ray crystallographic structure of the main protease of the SARS-CoV-2 (PDB ID: 7O46) and HIV virus (PDB ID: 1UUI) was retrieved from the protein data bank and used as receptor proteins. The molecular docking results showed that compounds (**LH_2-L^4H_2**) with SARS-CoV-2 and HIV virus exhibited good binding affinity at binding site of receptor protein. As potential drug candidates, Swiss-ADME and target predictions analyses are also studied and the results are compared with Chloroquine (CQ) and Hydroxychloroquine (HCQ) as anti-SARS-CoV-2 drugs.

Table 1 — Crystallographic data and refinement parameters for salen compound **LH_2**

Crystallographic data	Compound **LH_2**
Formula	$C_{16}H_{14}Br_2N_2O_2$
Mw (gmol^{-1})	426.09
temp (K)	220(2)
λ (Mo Kα),(Å)	0.71073
crystal system	Monoclinic
space group	$P2_1/c$
a (Å)	18.092(4)
b (Å)	7.1364(13)
c (Å)	6.1092(11)
α (°)	90
β (°)	93.514(5)
γ (°)	90
V (Å^3)	787.3(3)
Z	2
D_{calc} (Mg/cm^3)	1.797
μ (mm^{-1})	5.156
F(000)	420
Crystal size(mm^3)	0.200×0.120×0.050
Index ranges	-24<=h<=24, -9<=k<=9, -8<=l<=8
Collected reflections	26375
unique reflections	1972
Absorption correction	Semi-empirical from equivalents
max and min trans	0.745 and 0.382
Refinement method	Full-matrix least-squares on F^2
Goodness-of-fit (GOF) on F^2	1.056
R1 [$I > 2\sigma(I)$]^a	0.0606
wR2 (all data)^b	0.1979
CCDC Number	2176825

$^aR_1 = \sum||F_o| - |F_c||/\sum|F_o|$; $^bwR_2 = \{\sum[w(F_o^2 - F_c^2)^2]/\sum[w(F_o^2)^2]\}^{1/2}$

Hirshfeld surface analysis

An intermolecular interaction of the **LH_2** ligand was analyzed using Hirshfeld surfaces and fingerprint graphs. The Hirshfeld surface analysis is a tool for visualizing and evaluating the intermolecular interactions present in the transparent system of

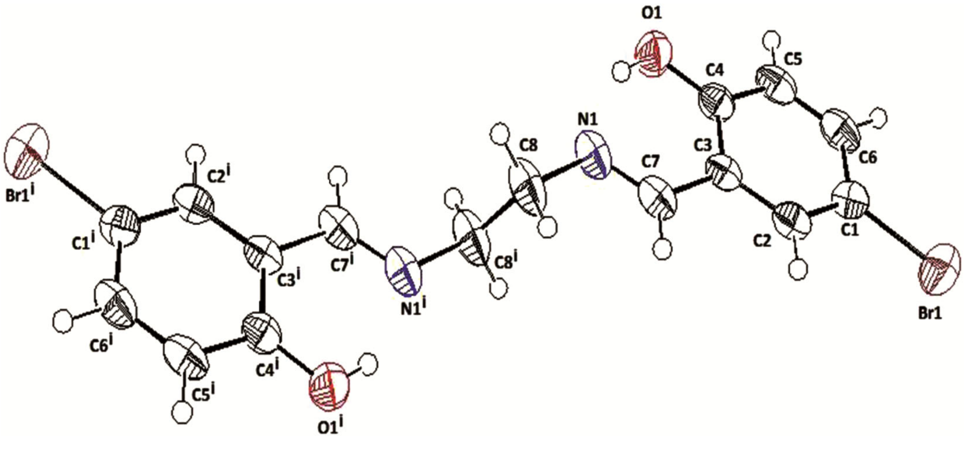

Fig. 1 — ORTEP diagram of the salen-type compound **LH_2** with 50% thermal ellipsoid and with atom numbering scheme. Hydrogen atoms are omitted for clarity

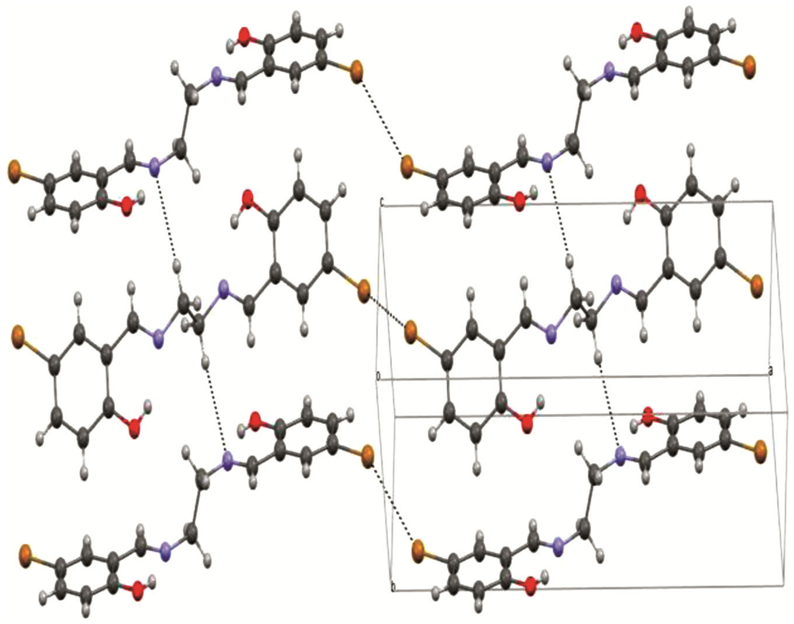

Fig. 2 — Unit cell packing diagram of the salen-type compound **LH$_2$** viewed down the a-axis

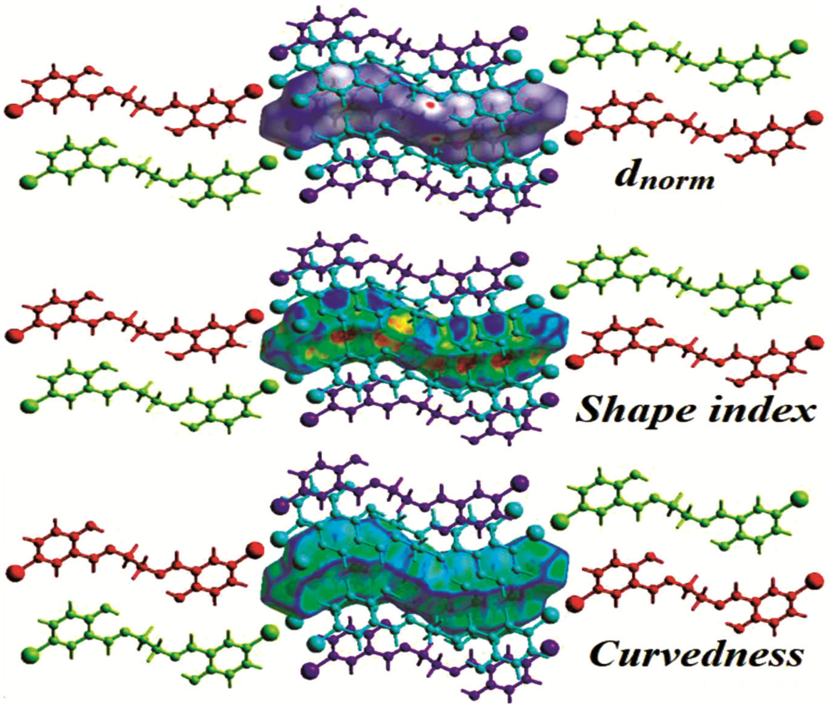

Fig. 3 — Graphical view of theHirshfeld surfaces mapped with d$_{norm}$ property; red spots represent the closest contacts and blue colour the most distant contacts for compound **LH$_2$**

organic ligand. Molecular Hirshfeld a surface in the crystal structure was constructed on the basis of the electron distribution calculated as the sum of spherical atom electron densities[18]. The molecular Hirshfeld surfaces (HSs) and their associated two-dimensional fingerprint plots (FPs) was generated for ligand **LH$_2$** based on their crystallographic information file (cif), using *CrystalExplorer 17.5* software[28]. Hirshfeld shape index, d$_{norm}$, d$_e$, d$_i$, fragment patch and curvedness surfaces of salen-type compound **LH$_2$** was presented in Fig. 3 and Fig. 4. Thestudy of d$_{norm}$ plot is used to identify the distance to the surface from

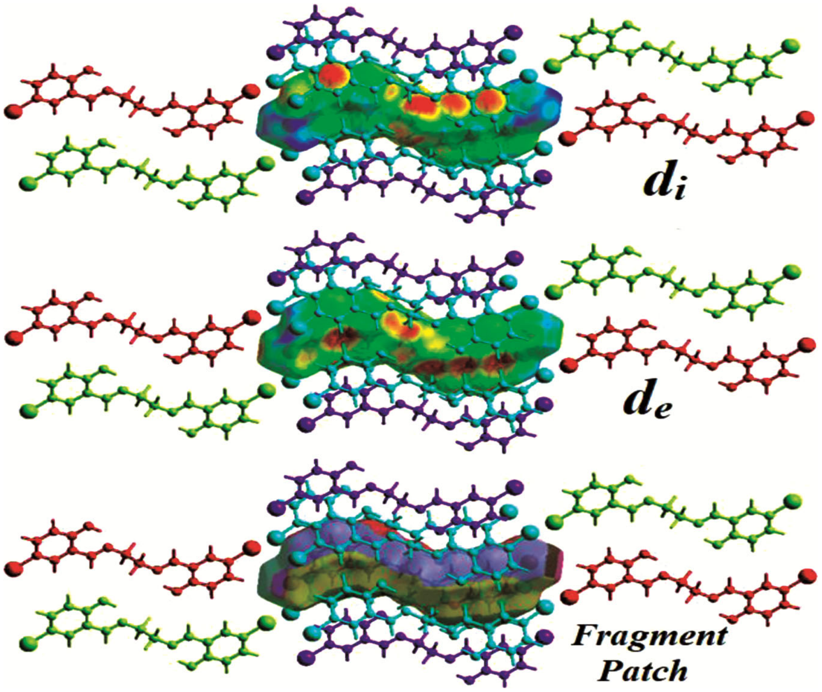

Fig. 4 — Graphical view of theHirshfeld surfaces mapped with d_{norm} property along with d_i, $d_e$and Fragment Patch; red spots represents the closest contacts and blue color the most distant contacts for compound **LH_2**.

nuclei outside and inside the Hirshfeld surface (*de* and *di*)[19]. Shape-index is mapped in the range of color -1.5 au (concave), 1.5 au (convex) represented by a red and blue "triangles" pattern and the curvedness plot lies in the range of -4.0 au (flat) which is represented by a flat region in the same zone of the surface. The d_{norm} surfaces displayed the contacts with distances equal to the sum of the van der Waals radii are represented as white regions and the contacts with distances shorter than and longer than van der Waals radii are shown as red circles and blue areas, respectively. Fig. 5 shows the decomposed characteristic fingerprint plots with significant percentage contributions of various intermolecular contacts to the HSs are represented in 2D plotted for salen-type compound **LH_2**; C…H ($d_e + d_i$ =3.4 Å), H…H ($d_e + d_i$ =2.4 Å), H…Br ($d_e + d_i$ =4.0 Å),O….H ($d_e + d_i$ =3.0 Å), Br…Br ($d_e + d_i$ =3.6Å), N…H ($d_e + d_i$ =3.1Å); d_i and d_e are the distances from the surface to the nearest atoms interior and exterior to the surface respectively. The 2D fingerprint plots and its reciprocal contacts associated with salen-type Schiff base compounds (**LH_2**) was shown in the range of 0.5-2.8 Å. It represents the complementary regions in plots and it can be predicted where one molecules behave as donor (de>di) while other behaves as an acceptor (de<di). It also It gives a quantitative summary of the nature and type of intermolecular contacts. The two-dimensional fingerprint plots generated corresponding to the H….H, C….H, H….Br, O….H, Br….Br, and N….H for compound **LH_2**. The H….H intermolecular contact is observed to be most and accounts for 28.5% of total HS for compound **LH_2**. The proportion of other significant intermolecular interaction C….H/H….C, for compound **LH_2** is found to be 27.3%. Further, H….Br (18.7%), O….H (9.9%), Br….Br (8.2%), N….H (2.9%) are the weak interaction of total HS for compound **LH_2**. Fig. S10 display the HS mapped with crystal void and deformation density of the ligand. The crystal-void calculation shows the void volume of the studied compound to be of the order of 458.14 Å and surface area in order of 186.42 Å. With the porosity, the calculated volume of crystal void is 22%. Deformation density maps of organic ligand allow studying the structural distribution of the electrons involved in the chemical bonding. The electron density deformation can be stated between the electronic clouds of the molecule, minus the electronic cloud of the promolecule. The deformation density is therefore positive between the bonds and negative at the nucleus. The strengths of interaction and 3D topology of the crystal packing was visualized through an energy framework[20]. Energy framework

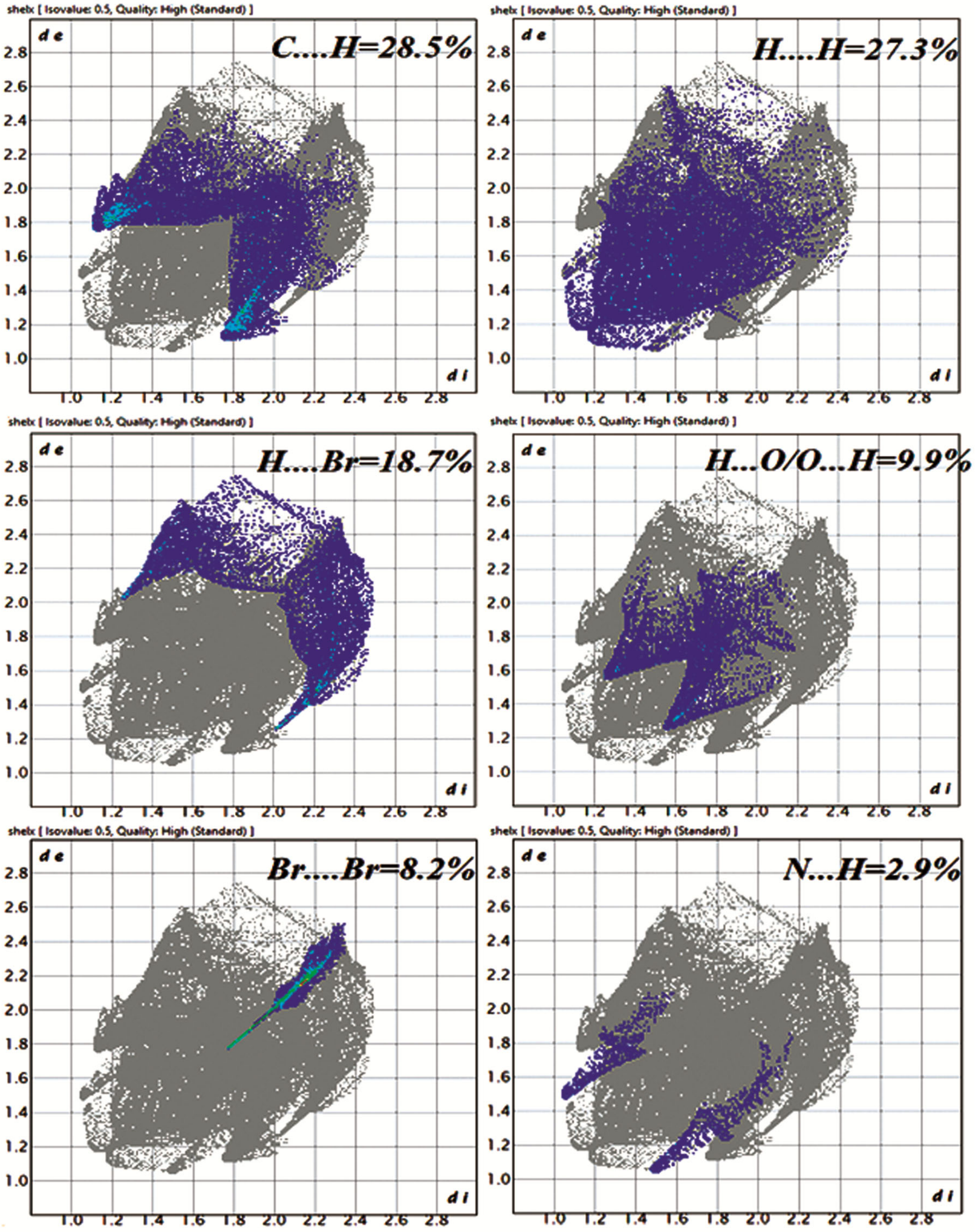

Fig. 5 — Decomposed characteristic fingerprint plots with significant percentage contributions of various intermolecular contacts to the HSs are represented in 2D plotted for compound **LH_2**; C…H ($d_e + d_i$ =3.4 Å), H…H ($d_e + d_i$ =2.4 Å), H…Br ($d_e + d_i$ =4.0 Å),O….H ($d_e + d_i$ =3.0 Å), Br…Br ($d_e + d_i$ =3.6Å), N…H ($d_e + d_i$ =3.1Å); d_i and d_e are the distances from the surface to the nearest atoms interior and exterior to the surface, respectively

analysis is a unique and advanced technique for the better understanding the nature of intermolecular interaction energies between the pair of organic ligand (**LH_2**) molecules with a 3-D graphical representation of their magnitude (Fig. 6). Hydrogen atoms have been omitted for clarity and all diagrams used the same hexagonal scale of 200 for energies. The interaction energies forLH_2 was calculated with CE-B3LYP/6-31G (*d*, *p*)] model displayed in Table S11. It is suggested that the total energy consists of pair wise individual energy profiles such as E_{coul}, E_{dis}, E_{tot} and $E_{tol.annot}$. The tube size (200) connecting the centroids of the molecule represent the relative strength of the interaction, and tube color represents types of energy profiles of the intermolecular interaction energies. The lattice energy was calculated using the result obtained was found to be -178.3 kJ/mol.

Quantum computational analysis

The geometry optimization and further modification of all synthesized salen-type Schiff base compounds (**LH_2-L^4H_2**) were carried out using B3LYP/DFT[21] conjugated with the basis set (6-311+G(d,p)). Fig. S12 shows the optimized and molecular structures of salen-type Schiff base compounds (**LH_2-L^4H_2**) derived from DFT methods. The frontier molecular orbital (FMO) analysis provides the parameters for calculating the FMO energy gap which is used for describing the electronic structure of the compounds. The FMO energies and FMO energy gap (E_{HOMO}-E_{LUMO}: ΔE) are the important parameters (Fig. S13 and S14) of molecular electronic structures for the studied salen-type Schiff base compounds (**LH_2-L^4H_2**). In each compounds, the HOMO electron densities are distributed mainly over chlorine and oxygen atoms of salicylaldehyde moiety while the LUMO electron densities are distributed over the entire azomethine moiety. The relatively higher HOMO energy of the salen-type Schiff base compounds (**LH_2-L^4H_2**) shows its electron donating ability. During HOMO-LUMO analysis, the relevant occupied and unoccupied MOs (HOMO/LUMO, HOMO-1/ LUMO+1 and HOMO-2/LUMO+2) are considered. The relevant HOMO-LUMO energies and energy gaps are shown in Table 2. In computer-aided drug design, molecular electrostatic potential (MEP) is used globally as a reactive map displaying the most suitable region for the electrophilic and nucleophilic attack of charged point-like reagents on organic molecules[22]. The calculated molecular electrostatic potentials (MEPs) maps and electron density surfaces of all the synthesized salen-type Schiff base compounds (**LH_2-L^4H_2**) are given in Figure S15 and S16 which illustrates the three-dimensional charge distributions within the molecules. Electrostatic potential map is drawn in the range -1.04 eV to -1.72 eV. Electrostatic potential map of the salen-type Schiff base compounds (**LH_2-L^4H_2**) reflects the electron donating character (red color) for Cl/O atoms of salicylaldehydes and N of azomethine moiety in the compounds. The different values of electrostatic potential are represented by different colours, with potential increases in the order: red < orange < yellow < green < blue. The red colour displays the maximum negative area, which shows favorable sites for electrophilic attack, the blue colour indicates the maximum positive area favourable for the nucleophilic attack, and the green colour represents zero potential area (Fig. S15 and S16). The global reactivity descriptors (units in eV), such as ionization potential (IP), electron affinity (EA), electro negativity (χ), chemical potential (μ), global hardness (η), global softness (σ) and global electrophilicity (ω), were calculated using the formulas based on Koopmans theorem[23].

The values of the chemical reactivity parameters are listed in Table 3. Overall, the electron donating abilities were described by ionization potential and electron affinity. The Global reactivity parameters (GRPs) explicated that all the synthesized salen-type Schiff base compounds (**LH_2-L^4H_2**) showed greater electron affinity (EA) than the ionization potential (IP); hence,

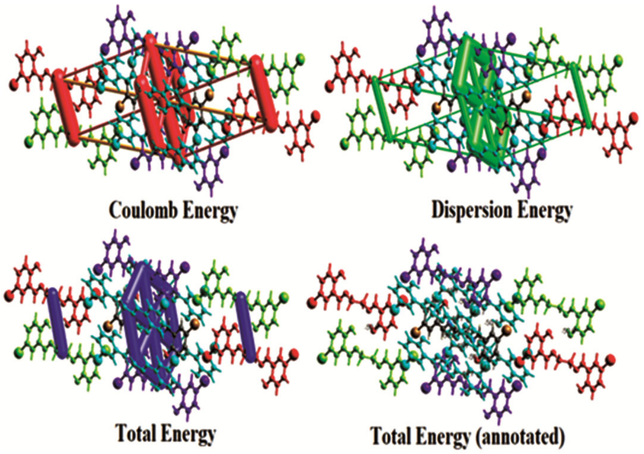

Fig. 6 — Energy Framework diagrams for compound **LH_2** along with Coulomb energy (E_{coul}), Dispersion energy (E_{dis}), Total energy (E_{tot}) and Total energy annotated ($E_{tot(annot)}$) for cluster of molecule in the compound **LH_2**. Hydrogen atoms have been omitted for clarity and all diagrams used the same hexagonal scale of 200 for energies

Table 2 — The computed HOMO and LUMO energies and the energy gap (ΔE)[a] of salen-type Schiff base compounds(**LH_2-L^4H_2**)

Molecular descriptors	LH_2	L^1H_2	L^2H_2	L^3H_2	L^4H_2
E_{LUMO}	–5.262	–4.827	–5.297	–5.124	–5.102
E_{HOMO}	–2.311	–2.218	–2.451	–2.213	–1.418
ΔE	–2.951	–2.609	–2.846	–2.911	–3.684
$E_{LUMO\ (+1)}$	–4.861	–6.597	–4.254	–3.851	–5.612
$E_{HOMO\ (-1)}$	–1.824	–0.657	–1.543	–1.231	–2.594
ΔE	–3.037	–5.940	–2.711	–2.620	–3.018
$E_{LUMO\ (+2)}$	–6.318	–4.453	–7.359	–7.126	–4.184
$E_{HOMO\ (-2)}$	–3.142	–1.214	–0.743	–3.611	–0.891
ΔE	–3.176	–3.239	–6.616	–3.515	–3.293

Table 3 — The computedGlobal reactivity descriptors of the salen-type Schiff base compounds (**LH_2-L^4H_2**)

Molecular descriptors	Mathematical description	**LH_2**	**L^1H_2**	**L^2H_2**	**L^3H_2**	**L^4H_2**
Ionization potential (IP)	$IP = - E_{HOMO}$	2.311	2.218	2.451	2.213	1.418
electron affinity (EA)	$EA = -E_{LUMO}$	5.262	4.827	5.297	5.124	5.102
electro negativity (χ)	$\chi = (IP + EA)/2$	3.786	3.522	3.874	3.668	3.260
chemical potential (μ)	$\eta = (IP - EA)/2$	-1.475	-1.304	-1.423	-1.455	-1.842
global softness (σ)	$\mu = -(IP + EA)/2$	-3.786	-3.522	-3.874	-3.668	-3.260
global hardness (η)	$\sigma = 1/2\eta$	-0.338	-0.383	-0.351	-0.343	-0.271
Electrophilicity index (ω)	$\omega = \mu^2 / 2\,\eta$	-4.858	-4.756	-5.273	-4.623	-2.884

they have greater electron-donating ability. The stability as well as reactivity of a chemical system was correlated to chemical potential and global hardness values. The stability had a direct relation with global hardness, whereas it had an inverse relationship to its reactivity. Thus, from the result obtain we can conclude that these compounds are most stable having highest global hardness (Table 3).

NMR and X-ray model quality of SARS-CoV2 M^{pro}

The recognition of errors in experimental and theoretical models of protein structures is a major problem in structural biology[24]. It provides an easy-to-use interface to the auto dock program which is frequently employed in protein structure validation. It calculates an overall quality score for a specific input structure. If this score is outside a range characteristic for native proteins the structure probably contains errors. A plot of local quality scores points to problematic parts of the model which are also highlighted in a 3D molecule viewer to facilitate their detection. It uses only the C-alpha atoms of the input structure, hence it can also be applied to low resolution structures and approximate models obtained early in the structure determination process. The *z*-score (*Z*-Score =-7.42) indicates overall model quality (Figure S17). Its value is displayed in a plot that contains the *z*-scores of all experimentally determined protein chains in current PDB (Figure S17). In this plot, groups of structures from different sources (X-ray, NMR) are distinguished by different colours (Fig. S17). It can be used to check whether the *z*-score of the input structure is within the range of scores typically found for native proteins of similar size. Plot of residue scores shows local model quality by plotting energies as a function of amino acid sequence position *i*. In general, positive values correspond to problematic or erroneous parts of the input structure. A plot of single residue energies usually contains large fluctuations and is of limited value for model evaluation. Hence the plot is smoothed by calculating the average energy over each 40-residue fragment *s (i,i+39)*, which is then assigned to the 'central' residue of the fragment at position *i+19* (Fig. S17, thick line). A second line with a smaller window size of 10 residues is shown in the background of the plot (Fig. S17, thin line). Z-scores of all protein chains in PDB determined by X-ray crystallography (light blue) or NMR spectroscopy (dark blue) with respect to their length. The z-scores of SARS-CoV-2 (PDB ID: 7O46) for COVID-19 is highlighted as large dots. Energy plot of SARS-CoV-2 (PDB ID: 7O46) residue energies averaged over a sliding window are plotted as a function of the central residue in the window.

Molecular docking with SARS-CoV-2 M^{pro}

Besides, NMR and X-ray model quality of SARS-CoV2 M^{pro}, in this investigation, a series of the salen-type compounds (**LH_2-L^4H_2**) were studied in silico to highlight their possible binding energy and interaction modes with the main protease (M^{pro}) of SARS-CoV-2 (PDB ID: 7O46) virus for COVID-19. The interaction of SARS-CoV-2 main protease (M^{pro}) and the docking results comprises of different posses with corresponding binding energies were analysed into the Discovery Studio Visualizer. In order to find potent SARS-CoV-2 inhibitor, in-silico molecular docking and analysis of the compounds (**LH_2-L^4H_2**) have been performed using AutoDock Vina software. Asre-docking was done to predict the binding affinity and pose of the compounds (**LH_2-L^4H_2**) with SARS-CoV-2 main protease for COVID-19 (PDB ID: 7O46), the outcomes obtained from docking screening associated to the binding energy is summarized in Table 4. The docking results show that all the synthesized compounds are the most promising ligands (-7.4, -6.3, -6.5, -6. 8 and -8.1 kcal/mol), which bound with SARS-CoV-2 M^{pro} *via* many hydrophobic bonding, electrostatic and hydrogen interactions. The stronger binding was predicted between compounds (**LH_2-L^4H_2**) and receptor protein

Table 4 — The molecular docking results of the salen-type Schiff base compounds (**LH_2-L^4H_2**) with SARS-CoV-2 M^{pro}, and nucleotide HIV-1 RNA virus including the binding affinity, inhibition constant and different amino acid residues of main protease that interact with the compounds

		Binding affinity (kcal/mol)	Inhibition constant, Ki (μM)	Interacting protein residues		
				H-bond	Electrostatic	Hydrophobic
LH_2	7O46	–7.4	1.393	GLY-109 (2.53Å) THR-111 (3.65Å)	PHE-294 (2.33 Å) VAL-202 (3.69 Å)	ASN-203 (2.85Å) HIS-246 (3.96Å) THR-292 (4.37Å)
	1UUI	–7.8	4.239	U-25 (3.79 Å) A-22 (4.69 Å)	C-41 (4.31Å)	G-26 (3.98Å) G-21 (2.69Å)
	5YUX	–7.9	1.329	DA-867 (4.16 Å)	DG-868 (3.63Å)	DT-866 (2.96 Å)
L^1H_2	7O46	–6.3	0.856	GLU-166 (2.63Å)	HIS-41 (3.51Å)	MET-49 (5.22Å), MET-165 (4.54Å), ARG-188 (4.77Å), GLN-189 (2.31Å)
	1UUI	–7.3	6.613	A-20 (4.41Å), G-18 (3.20Å)	C-19 (5.07Å), C-44 (4.89Å)	G-43 (3.41Å), U-42 (2.68Å), G-21 (5.04Å)
	5YUX	–7.3	5.291	DG-868 (3.98Å)	DA-867 (6.21Å)	DG-869 (2.31Å), DT-866 (3.56Å)
L^2H_2	7O46	–6.5	1.958	ASN-142 (3.49Å) HIS-164 (3.22Å)	HIS-41 (2.89Å), THR-190 (4.26Å)	ARG-188 (2.48Å), PRO-168 (4.77Å), CYS-145 (3.95Å), MET-165 (4.13Å)
	1UUI	–8.2	2.601	A-20 (2.94Å), G-43 (5.12Å)	C-44 (2.41Å), C-19 (5.67Å)	G-21 (4.48Å), U-42(2.86Å)
	5YUX	–7.5	4.216	DG-868 (4.19Å)	DG-849 (3.11Å)	DT-866 (4.83Å), DA-867 (5.19Å)
L^3H_2	7O46	–6.8	3.191	GLN-189 (3.71Å), HIS-164 (2.55Å)	LEU-167 (4.42Å)	PRO-168 (3.60Å), ARG-188 (2.65Å), HIS-164 (3.55Å), CYS-145 (5.29Å)
	1UUI	–6.9	5.452	G-43 (4.94Å), U-42 (2.79Å)	C-41 (4.13Å) G-18(2.45Å)	A-22 (4.93Å), G-21 (5.31Å), U-40(3.67Å)
	5YUX	–7.4	8.134	DG-868 (3.99Å)	DG-866 (2.16Å)	DG-869 (3.63Å), DA-867 (5.34Å)
L^4H_2	7O46	–8.1	4.658	GLU-166 (3.15Å), GLN-189 (5.28Å), ASN-142 (2.89Å)	MET-49 (4.52Å), HIS-41 (3.13Å)	SER-144 (3.41Å), MET-165 (3.82Å), CYS-145 (3.47Å)
	1UUI	–8.4	1.891	A-20 (4.23Å), G-43 (2.97Å), U-40 (3.19Å)	C-41 (4.83Å), C-44 (3.98Å)	G-18 (2.45Å), C-19 (3.79Å), A-22(2.33Å)
	5YUX	–7.6	9.563	DG-868 (5.14Å), DA-867 (4.93Å)	DT-844 (5.23Å) DC-845 (4.81Å)	DG-869 (3.12Å) DC-846 (4.63Å)

through negative value of binding affinity. The representation of docked compounds inside the SARS-CoV-2 M^{pro} with its focused view for interacting different amino acid residues are displayed in Fig. 7 and Fig. 8. The molecular docking calculations of the **LH_2**into the main protease of SARS-CoV-2 for COVID-19 (PDB ID: 7O46) revealed the binding energy of -7.4 kcal/mol with an inhibition constant of 1.393 μM at inhibition binding site of receptor protein. There are seven amino acid residue interactions (GLY-109, THR-111, PHE-294, VAL-202, ASN-203, HIS-246, THR-292) between **LH_2** and main protease (M^{pro}) of the SARS-CoV-2 for COVID-19. The molecular docking calculations of the **L^1H_2** into the main protease of SARS-CoV-2 for COVID-19 (PDB ID: 7O46) resulted in the binding energy of -6.3 kcal/mol, and the inhibition constant of 0.856 μM. The docking study has exhibited that **L^1H_2** also interacted with six amino acid residues (GLU-166, HIS-41, MET-49, MET-165, ARG-188 and GLN-189). In compound **L^2H_2**, **L^3H_2**and**L^4H_2**,the molecular docking calculations resulted in the binding energy of -6.5, -6.8 and -8.1 kcal/mol with the inhibition constant of 1.958, 3.191 and 4.658 μM, respectively. The major amino acid residue interactions are ASN-142, HIS-164, HIS-41, THR-190, ARG-188, PRO-168, CYS-145, MET-165 for **L^2H_2**; GLN-189, HIS-164, LEU-167, PRO-168, ARG-188, HIS-164, CYS-145 for **L^3H_2**; GLU-166, GLN-189, ASN-142, MET-49, HIS-41, SER-144, MET-165, CYS-145 for**L^4H_2**.These binding energies of compounds (**LH_2-L^4H_2**) are reasonably well as compared to recently known antiviral drugs. For instant, the binding affinities of the compounds (**LH_2-L^4H_2**) (-7.4, -6.3, -6.5, -6. 8 and -8.1 kcal/mol) was found to be better than that of recently docking results of anti-SARS-CoV-2 drugs like chloroquine (-6.293 kcal/mol), hydroxychloroquine (-5.573 kcal/mol) and remdesivir (-6.352 kcal/mol) when targeted to the active-siteof SARS-CoV-2 M^{pro} for COVID-19[25,26]. These compounds may be used as anti-COVID-19(anti- SARS-CoV-2) drugs. The hydrogen bond interactions and intermolecular interactions was visualized[27,28] between of the compounds (**LH_2-L^4H_2**) with SARS-CoV-2 main protease for COVID-19 (PDB ID: 7O46). Fig. 9 and Fig. 10 shows docked compounds (**LH_2-L^4H_2**) docked into the binding cavity of the receptor protein interaction of COVID-19 M^{pro} (PDB ID: 7O46).The best docking poses of compounds in interaction with SARS-CoV-2 virus.

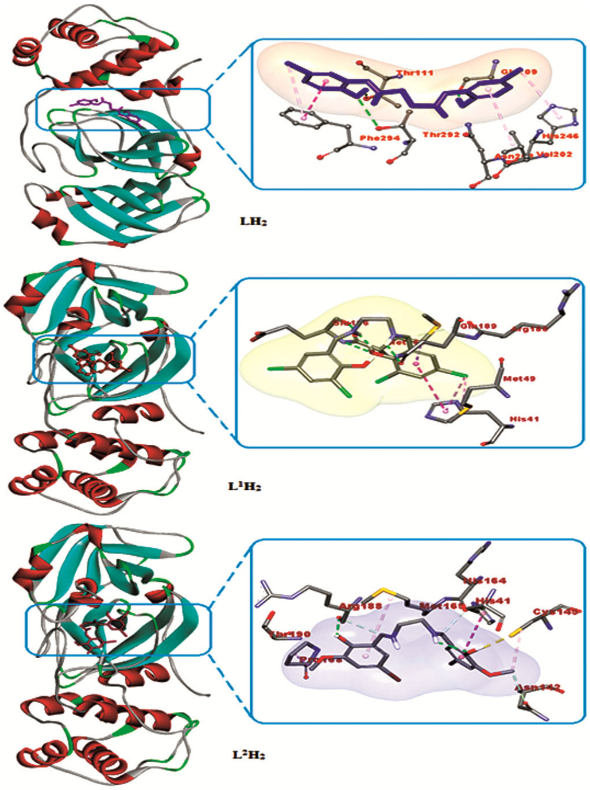

Fig. 7 — Docked salen-type compounds **LH_2, L^1H_2**and **L^2H_2** with SARS-CoV-2 M^{pro} (PDB ID: 7O46) in focused view for interacting residues

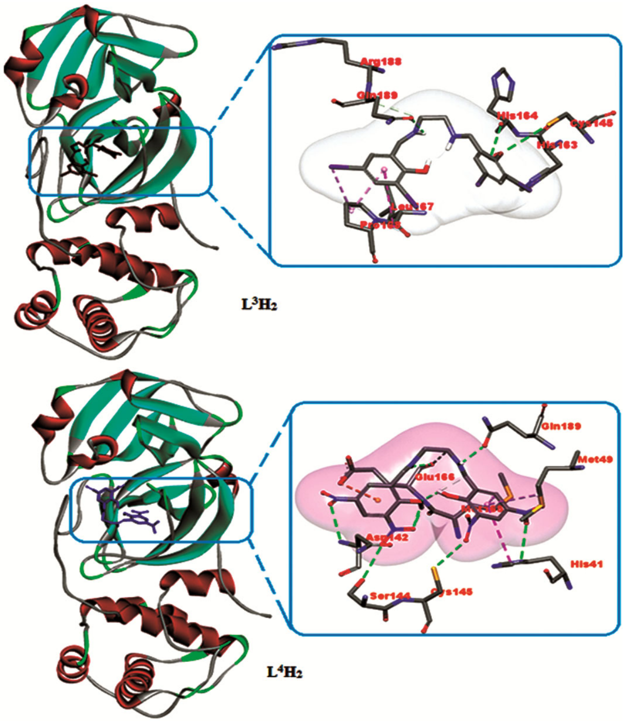

Fig. 8 — Docked compounds **L^3H_2** and **L^4H_2** with SARS CoV-2 (PDB ID: 7O46) in focused view for interacting residues

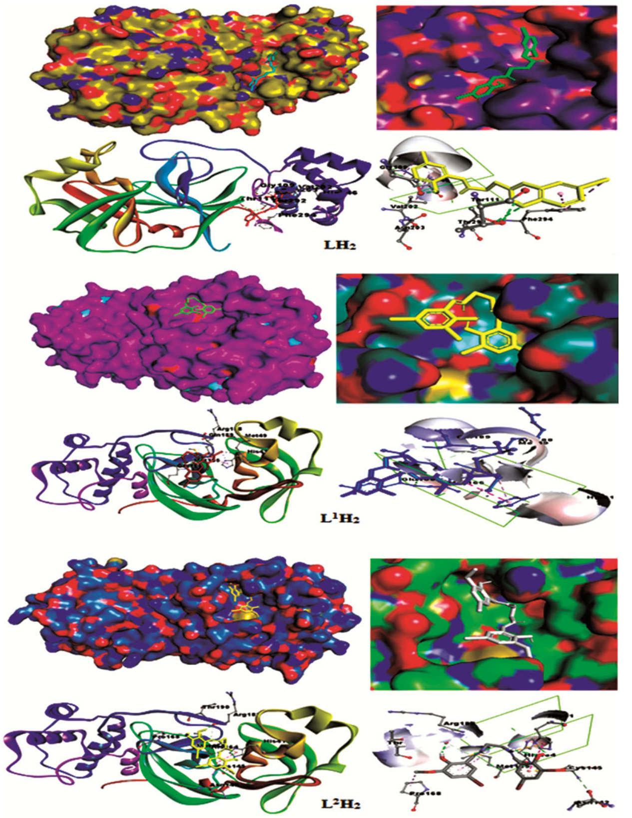

Fig. 9 — Docked compounds **LH_2**, **L^1H_2**and **L^2H_2** into the binding cavity of the receptor protein interaction of COVID-19 M^{pro} (PDB ID: 7O46). The best docking poses of compounds in interaction with SARS-CoV-2 virus. The molecular re-docking study showed in surface view and 3D protein backbone with ligand represented as a cartoon and corresponding 2D protein-ligand interaction plot

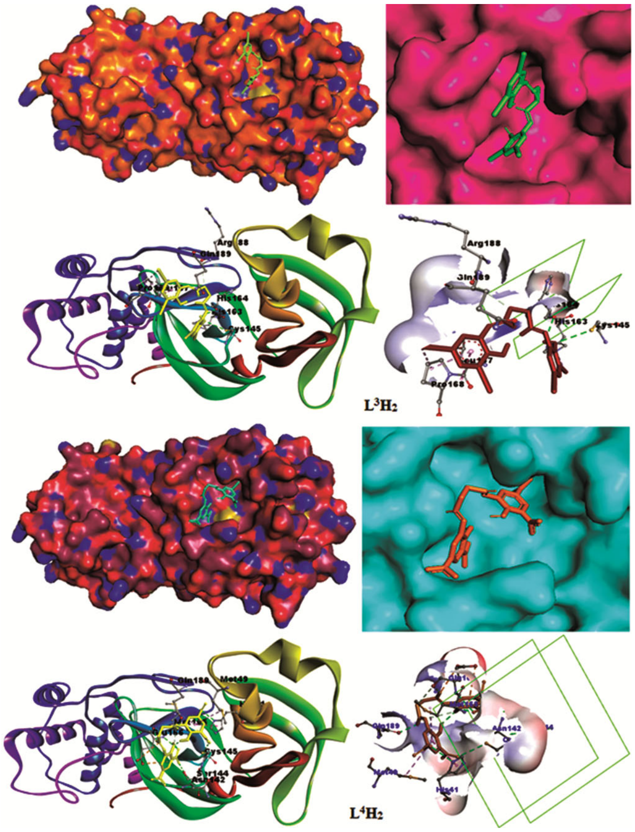

Fig. 10 — Salen-type compounds **L^3H_2**and **L^4H_2** are docked into the binding cavity of the receptor protein interaction of COVID-19 M^{pro} (PDB ID: 7O46).The best docking poses of compounds in interaction with SARS-CoV-2 virus. The molecular re-docking study showed in surface view and 3D protein backbone with ligand represented as a cartoon and corresponding 2D protein-ligand interaction plot

The molecular re-docking study showed in surface view and 3D protein backbone with ligand represented as a cartoon and corresponding 2D protein-ligand interaction plot. There existed two H-bonds (GLY-109, THR-111), two electrostatic interaction (PHE-294, VAL-202) and three hydrophobic interactions (ASN-203, HIS-246, THR-292) between the main protease of SARS-CoV-2 inside the docked ligand **LH_2**. In compound **L^1H_2**, there existed one H-bond (GLU-166), one electrostatic interaction (HIS-41) and four hydrophobic interactions (MET-49, MET-165, ARG-188, GLN-189) between the main protease of SARS-CoV-2 with the docked ligand **L^1H_2**. Similarly, two H-bonds (ASN-142, HIS-164), two electrostatic interaction (HIS-41, THR-190) and four hydrophobic interactions (ARG-188, PRO-168, CYS-145, MET-165) were seen between the main protease of SARS-CoV-2 with the docked ligand **L^2H_2**.Similar observations were observed for compound **L^3H_2** and **L^4H_2**. Graphical representation of docked Salen-type compounds (**LH_2-L^4H_2**) inside the SARS-CoV-2 M^{pro} with its focused view for interacting amino acid residues along with H-bond and intermolecular interactions are displayed in Figure S18 to S22. Also, two dimensional diagrams and Lig-Plot image for the interaction of compounds (**LH_2-L^4H_2**) with SARS-CoV-2 main protease (M^{pro}) are presented in Figure S23 and S24. Overall, our in-silico molecular docking study reveals that the synthesized novel compounds (**LH_2-L^4H_2**) may be considered as anti-COVID-19 (anti-SARS-CoV-2) drug candidates.

Molecular docking with HIV-1 RNA virus

The search for new anti-HIV drugs remains a major challenge in the scientific world. The genetic material of the virus composed of a single RNA strand which is identified as the largest among all the RNA viruses reported so far[29]. Once the virus infects the cell, its genome act as a messenger RNA (mRNA) and initiates the synthesis of polyproteins. These synthesized polyproteins helps the virus to replicate new viruses[30]. The polyproteins in terms make several RNAs, many more structural proteins that together contribute to the construction of a new virus[31]. As potent HIV protease inhibitors, Anti-Human Immunodeficiency virus (Anti-HIV) properties of a series of new salen-type Schiff base compounds (**LH_2-L^4H_2**) have been explored using in-silico molecular docking and analysis against HIV-1 RNA virus (PDB ID: 1UUI).The graphical representation of the salen-type compounds (**LH_2-L^4H_2**) inside the HIV-1 RNA virus with its focused view for interacting different nucleotide residues are displayed in Figure S25 to S29, and docking results along with H-bonding, electrostatic interaction and hydrophobic interaction are given in Table 4. The representation of docked salen-type compounds (**LH_2-L^4H_2**) inside the HIV-1 RNA with its focused view for interacting different nucleotide residues are given in Fig. 11 and Fig. 12. Fig. 13 and Fig. 14 shows the **m**olecular re-docking of the salen-type compounds (**LH_2-L^4H_2**) with focused view for nucleotide (RNA) interacting residues as Adenine(A), Guanine (G), Cytosine (C) and Uracil (U) of HIV-1 virus (PDB ID: 1UUI) around the docked ligands. The best docking poses of the salen-type compounds in interaction with HIV-1 RNA virus showed in surface view and 3D protein backbone with compounds represented as a cartoon and corresponding protein-ligand interaction plot around the docked ligands. Fig. 15 show the graphical representation for docked salen-type compounds

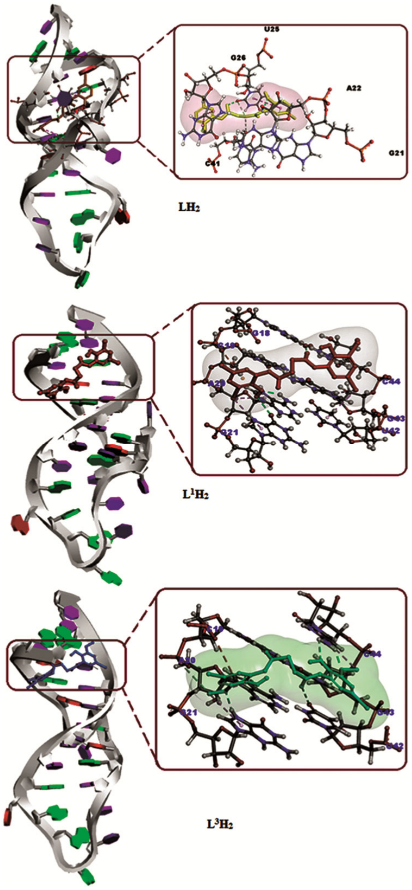

Fig. 11 — The salen-type compounds **LH_2, L^1H_2**and **L^2H_2** are docked into the binding cavity of the receptor protein interaction of HIV-1 virus (PDB ID: 1UUI)

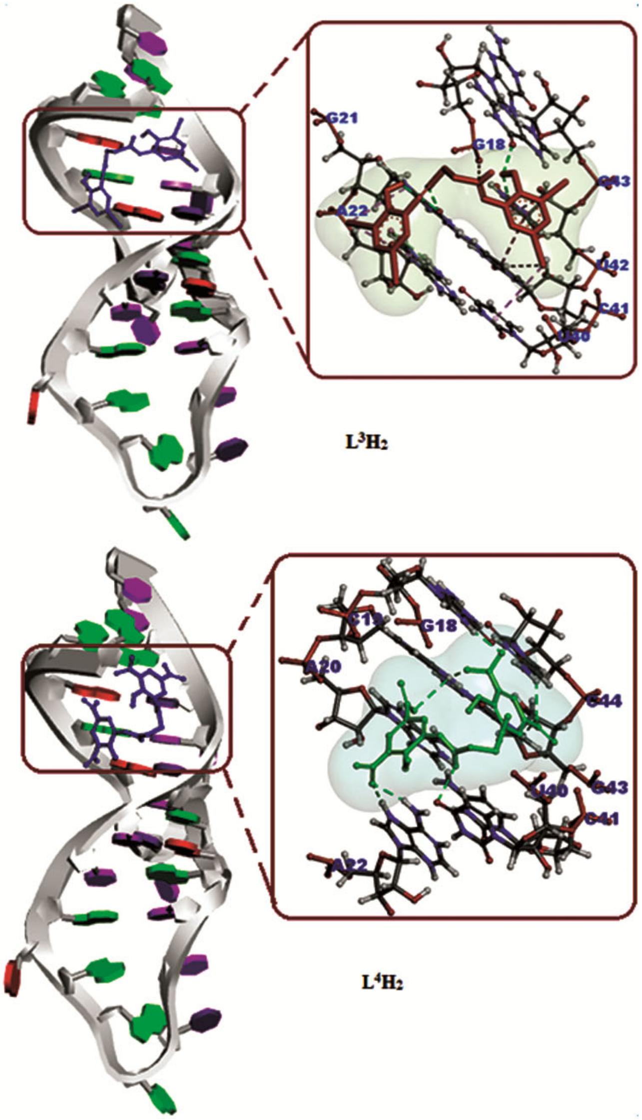

Fig. 12 — The salen-type compounds **L^3H_2**and **L^4H_2** are docked into the binding cavity of the receptor protein interaction of HIV-1 virus (PDB ID: 1UUI)

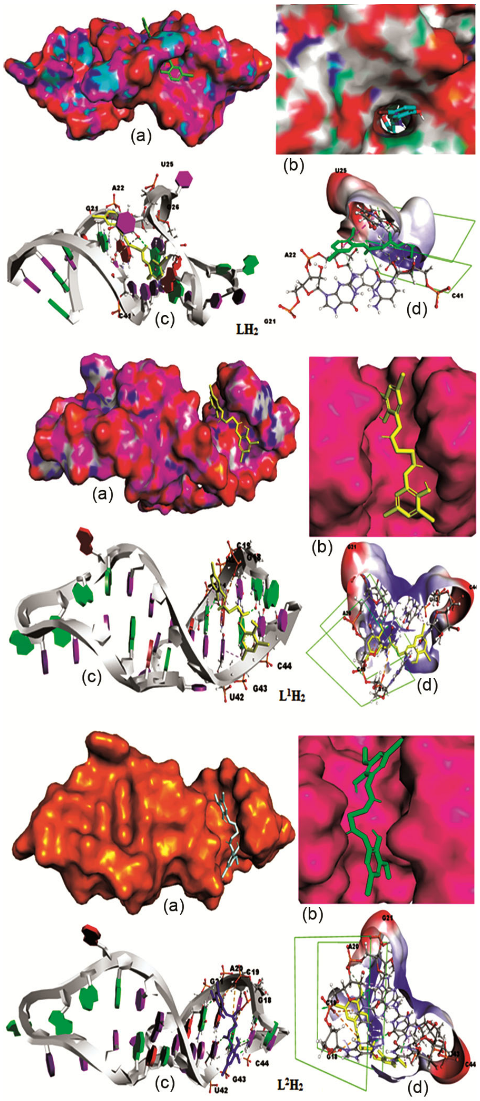

Fig. 13 — Molecular re-docking of the salen-type compounds **LH_2, L^1H_2** and **L^2H_2** with focused view for nucleotide interacting residues of HIV-1 virus (PDB ID: 1UUI).The best docking poses of the salen-type compounds **LH_2, L^1H_2** and **L^2H_2** in interaction with HIV-1 RNA virus showed in surface view and 3D protein backbone with compounds represented as a cartoon and corresponding protein-ligand interaction plot

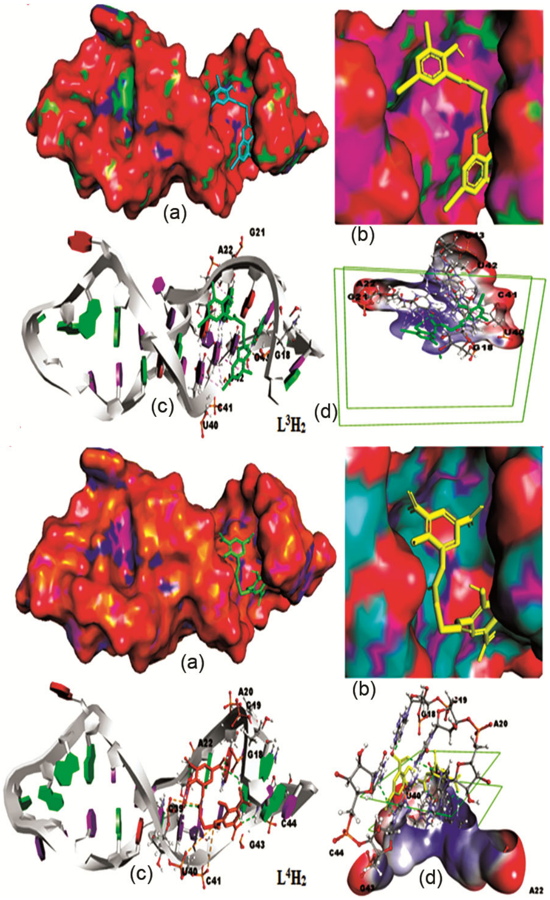

Fig. 14 — Molecular re-docking of the salen-type compounds **L^3H_2** and **L^4H_2** with focused view for nucleotide interacting residues of HIV-1 virus (PDB ID: 1UUI).The best docking poses of the salen-type compounds **L^3H_2** and **L^4H_2** in interaction with HIV-1 RNA virus showed in surface view, 3D protein backbone with compounds represented as a cartoon and corresponding protein-ligand interaction plot

(**LH_2-L^4H_2**) inside the HIV-1 RNA virus (PDB ID: 1UUI) with focused view for interacting RNA residues such as Adenine(A), Guanine (G), Cytosine (C) and Uracil (U) around the docked compounds. Selected nucleotide residue interactions between ligands and HIV-1 RNA virus (PDB ID: 1UUI) are: U-25, A-22, C-41, G-26, G-21 for **LH_2**; A-20, G-18, C-19, C44, G-43, U42, G-21 for **L^1H_2**; A-20, G43, C-44, C-19, G-21, U-42 for **L^2H_2**; G-43, U-42, C-41, G-18, A-22, G-21, U-40 for **L^3H_2**; A-20, G-43, U-40, C-41, C-44, G-18, C-19, A-22 for **L^4H_2** inside the docked ligands. The molecular docking study reveals that the **LH_2** exhibited the binding energy of -7.8 kcal/mol with an inhibition constant of 4.239 μM at inhibition binding site of receptor protein interaction of HIV-1 virus (PDB ID: 1UUI). In this compound, there existed two H-bond (U-25, A-22), one electrostatic interaction (C-41) and two hydrophobic interactions (G-26, G-21) between the HIV-1 RNA with the docked ligand **LH_2**. Similarly, the molecular docking study reveals that the salen-type compounds **L^1H_2, L^2H_2,L^3H_2**,and **L^4H_2** resulted the binding energy of -7.3, -8.2, -6.9 and -8.4 kcal/mol with an inhibition constant of 6.613, 2.601, 5.452 and 1.891 μM, respectively at receptor protein interaction of HIV-1 virus (PDB ID: 1UUI). As the molecular docking was done to predict the binding affinity and pose of the salen-type Schiff base compounds (**LH_2-L^4H_2**), the outcomes obtained from docking screening associated to the binding energy is summarized in Table 4. The hydrophobic bonding, electrostatic and hydrogen interactions between the salen-type compounds $\mathbf{L^1H_2}$, $\mathbf{L^2H_2}$,$\mathbf{L^3H_2}$,and $\mathbf{L^4H_2}$ and HIV-1 RNA are: there existed two H-bond (A-20, G-18), two electrostatic interaction (C-19, C-44) and three hydrophobic interactions (G-43, U-42, G-21) for $\mathbf{L^1H_2}$; two H-bonds (A-20, G-43), two electrostatic interaction (C-44, C-19) and two hydrophobic interactions (G-21, U-42) for $\mathbf{L^2H_2}$; two H-bonds (U-42, G-43), two electrostatic interaction (C-41, G-18) and three hydrophobic interactions (A-22, G-21, U-40) for $\mathbf{L^3H_2}$; three H-bonds (A-20, G-43, U-40), two electrostatic interaction (C-44, C-41) and three hydrophobic interactions (G-18, C-19, A-22) for $\mathbf{L^4H_2}$.

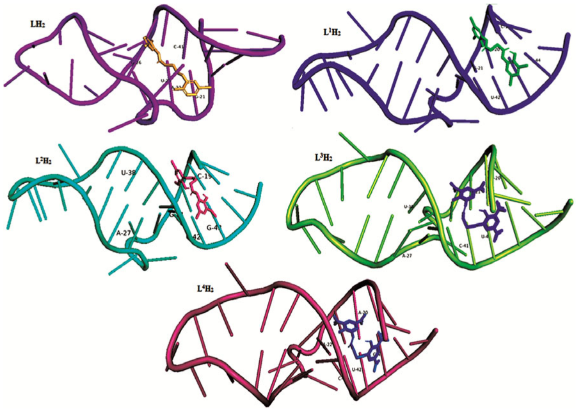

Fig. 15 — The graphical representation for docked salen-type compounds ($\mathbf{LH_2}$-$\mathbf{L^4H_2}$) inside the HIV-1 RNA virus (PDB ID: 1UUI) with focused view for interacting RNA residues such as Adenine(A), Guanine (G), Cytosine (C) and Uracil (U) around the docked compounds

The binding energy values obtained in docking calculations of the synthesized salen-type Schiff base compounds ($\mathbf{LH_2}$-$\mathbf{L^4H_2}$) are comparable with those of other anti-HIV compounds reported in the literature[32,33]. It was noted that thebinding affinities of the synthesized salen-type Schiff base compounds ($\mathbf{LH_2}$-$\mathbf{L^4H_2}$) against SARS-CoV-2 were comparatively lower (-7.4, -6.3, -6.5, -6. 8 and -8.1 kcal/mol) than towards the HIV virus (-7.8, -7.3, -8.2, -6. 9 and -8.4 kcal/mol).

Molecular docking with DNA polymerase IV as receptor

Molecular docking is an interesting tool which is used to predict the DNA interactions of salen-type compounds. These compounds can attach in different modes to a specific binding site of a DNA receptor[34]. The lowest energy conformations were rated based on docking calculations of the lowest free binding energy. The minimum energy of each compound was applied inside the DNA polymerase IV (PDB ID: 5YUX) as a receptor. Re-docking has also been performed to validate our molecular docking protocols and results are given in Table 4. Fig. 16 and Fig. 17 showsdocked ligands inside the DNA polymerase IV (PDB ID: 5YUX) with its interacting nucleotide residues around the docked DNA model and surface representation. The molecular docking study reveals that the LH_2exhibited the binding energy of -7.9 kcal/mol with an inhibition constant of 1.329 μM. Similarly, the molecular docking calculations of the$\mathbf{L^1H_2}$-$\mathbf{L^4H_2}$ with DNA polymerase IV (PDB ID: 5YUX) also resulted in the binding

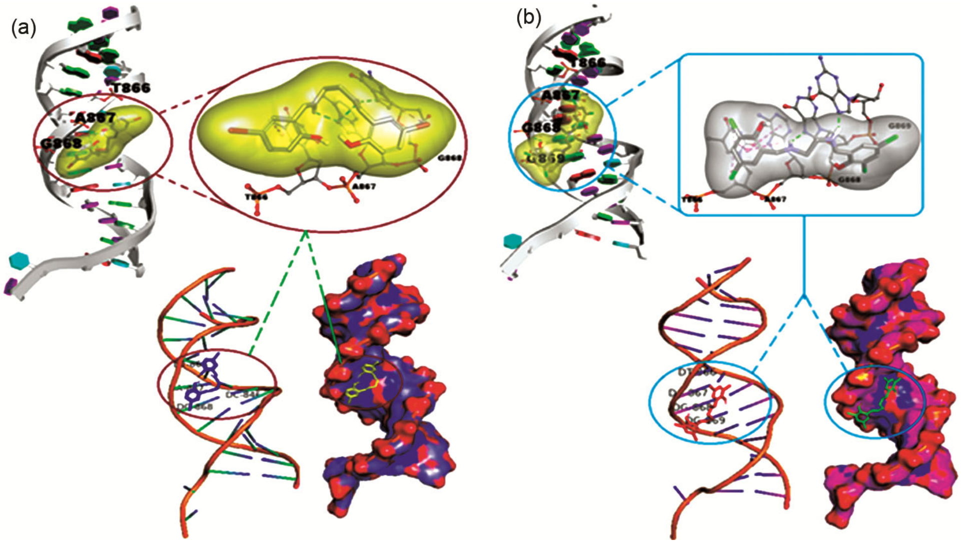

Fig. 16 — (A) Docked ligand LH_2; (B) docked ligand L^1H_2 inside the DNA polymerase IV (PDB ID: 5YUX) with its interacting nucleotide residues around the docked DNA model and surface representation

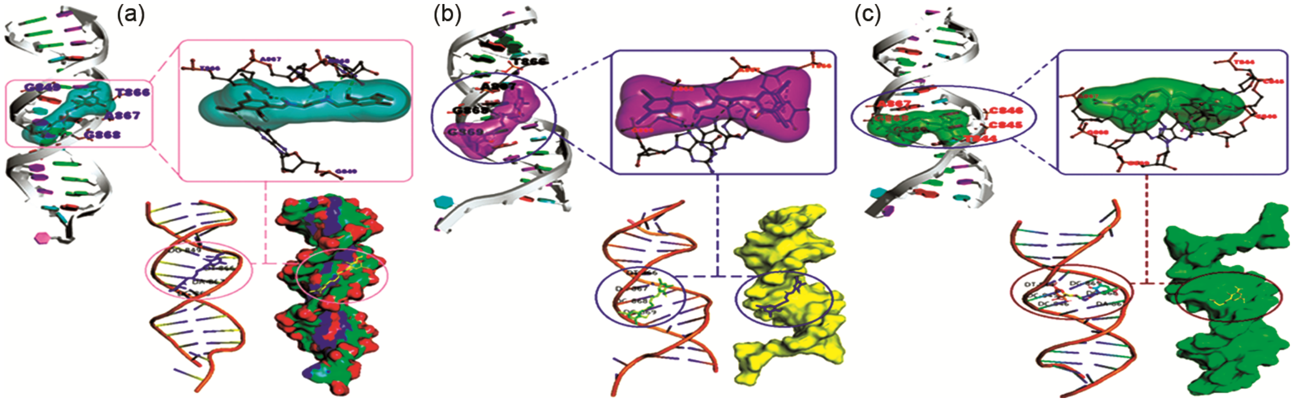

Fig. 17 — (A) Docked ligand L^2H_2; (B) docked ligand L^3H_2 and (C) docked ligand L^4H_2 inside the DNA polymerase IV (PDB ID: 5YUX) with its interacting nucleotide residues around the docked DNA model and surface representation

energy of the range -7.3 to -7.6 kcal/mol, and the inhibition constant of the range 4.216-9.563 µM. There is single Hydrogen bonding interactions between the NH_2 group of LH_2 and the phosphate oxygen atoms of DNA helix at 4.16 Å. On the other hand, $\mathbf{L^1H_2}$-$\mathbf{L^4H_2}$ interacted with DNA through Hydrogen bonding with DG-868 (3.98 Å), DG-868 (4.19 Å), DG-868 (3.99 Å), and DG-868 (5.14 Å) and DA-867 (4.93Å) respectively. According to data from molecular docking methods, positive electron density on the surface of compounds facilitates the ligand-drug's access to DNA phosphate groups[35]. The DNA docking data for studied compounds indicated that they had a high affinity for binding to the target DNA duplex.

Simulation and modeling study

We perform extensive classical molecular dynamics simulation to investigate the consequences of docking of the synthesized Ligand $\mathbf{LH_2}$ on a protein moiety(PDB ID: 7O46)[36] as mentioned earlier. For the simulation purpose we construct a cubic simulation box of edge length ~10 nm by placing the protein at the center of the box. We generate two systems for this simulation study namely, WP: Wild Protein in water (represented in orange), PL: Protein-ligand complex in water (represented in blue). The aforementioned color codes for these two systems are maintained throughout the simulation study. The position of the protein is kept constant by applying force of 1000 kJ mol^{-1} nm^{-2} on the heavy atoms of the protein from all three directions. Whereas, for the PL system position restrain is applied on both protein and ligand molecule simultaneously. Subsequently the simulation box is filled with water molecules using gmx solvate tool of GROMACS[37]. Detailed information for each system is provided in the Table 5.

Table 5 — Details of the composition of different systems and their simulation length

System Name	Number of Protein	Number of Ligand	Number of Water	Simulation Time (ns)
WP	1	–	30314	100
PL	1	1	30308	100

Furthermore, we start by checking the stability of systems (WP, PL here) by employing Root Mean Square Deviation (RMSD) considering the entire length of the trajectory *i.e.* 100 ns. We probed the stability of the docked drugs, $\mathbf{LH_2}$ in the active pocket and its effects on the stability of the whole system. It immediately follows from Fig. 18 that the time evolution of the average RMSD for the C_α atoms of the protein moiety mostly does not go beyond 0.25 nm in pure water indicating its stability in native conformation (Left panel, WP, orange curve).The figure also indicates that all systems are stable within an acceptable range of deviation especially if considered as the final 50 ns of the simulated trajectory. The average RMSD for the systems (WP and PL) is found to be between 0.15 and 0.25 nm. C_α atoms of the protein (WP) exhibit an average RMSD of 0.2 nm soon after reaching 50 ns and the system stability remains uniform for the rest of the simulated trajectory. It is evident that when ligand $\mathbf{LH_2}$ is docked with the protein under investigation the complex (PL, blue curve) remains stable, and show an acceptable deviation around and average RMSD value of 0.175 nm. As a consequence of docking the backbone gains stability 30 ns onwards and exhibits very little fluctuation which sheds light on the fact that the ligand remained intact, and the system entered

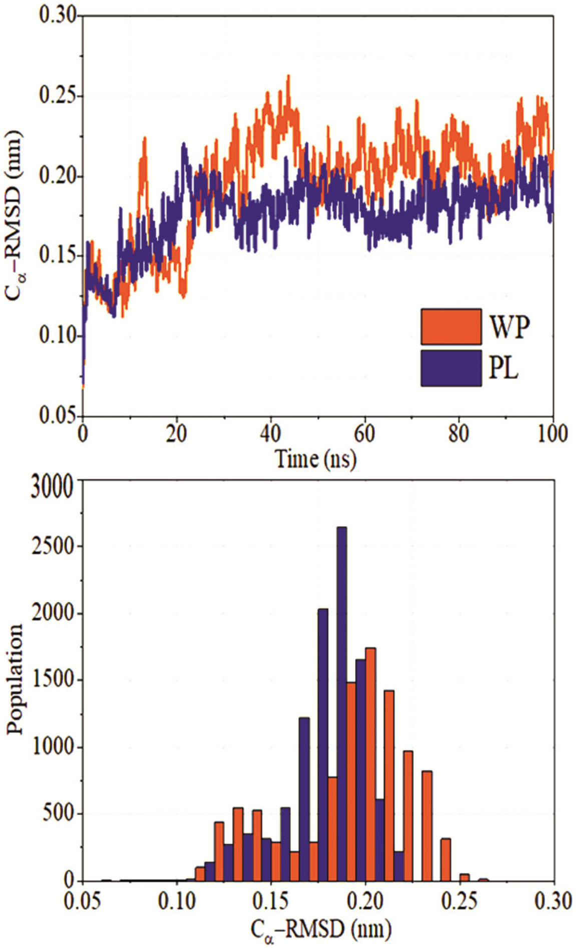

Fig. 18 — Time evolution (left panel) and population (right panel) of average RMSD for the C_α atoms of 7O46 for two systems namely, WP (orange) and PL (blue)

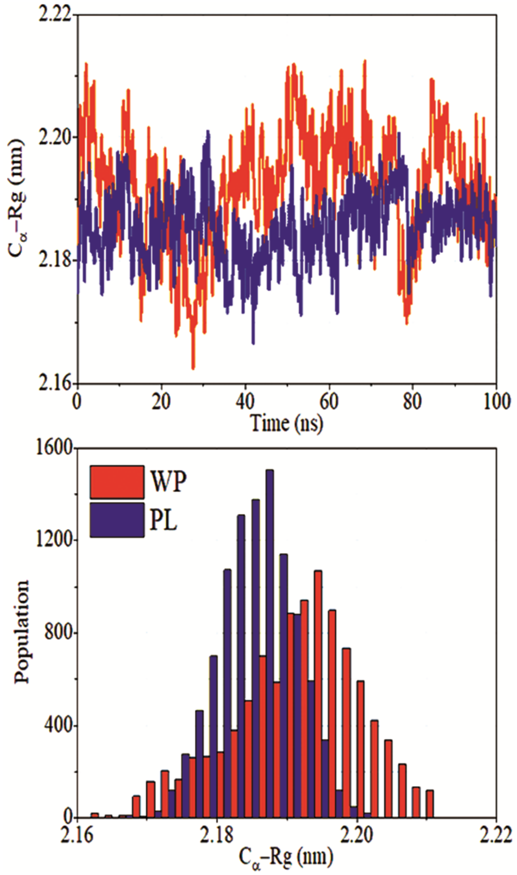

Fig. 19 — Time evolution (left panel) and population (right panel) of Rg for the C_α atoms of 7O46 for two systems namely, WP (orange) and PL (blue)

the production phase soon when compared to the WP and is evident from Fig. 18 (Left panel, PL, blue curve). The differences in the RMSD observed are arisen owing to the binding and unbinding of the ligand at different time intervals. Next to the time evolution of average RMSD we represent the histogram of the time series to have an idea regarding the population of the protein structure at different sampled states. It is clear from the histogram analysis (Fig. 18, right panel) that while LH_2 is docked with protein backbone (Right panel, PL, blue bar) average RMSD mostly stays within 0.15 to 0.2 nm whereas the native structure of the protein (Right panel, WP, orange bar) samples over a wide range of RMSD values compared to WP. Hence, we witness stable internal motions and negligible fluctuations during the course of the simulation for system PL. The radius of Gyration (Rg) depicts the information regarding the stable and unstable folding of the protein moiety while interacting with ligands. Low Rg values indicate greater compactness and higher structural stiffness (more folded) and *vice-versa*. Thus, calculations of Rg assess the system's compactness over time. As evident from Fig. 19, although the time evolution of Rg for the systems show fluctuation a little higher, the essence of the outcome lies in the fact that in the presence of the ligand LH_2, protein backbone shows higher packing compared to its absence. The binding and unbinding of the ligand impacts greatly to the overall compactness of the complexes. The time evolution of the simulated complex (Left panel, PL, blue curve) show Rg values mostly stay around 2.18 nm whereas native protein exhibits higher fluctuation in the range 2.19 nm. Next to the time evolution of average Rg we place the histogram of the time series to have an idea regarding range of sampled states. It is clear from the histogram analysis (Fig. 19, right panel) that while LH_2 is docked with the protein backbone (Right panel, PL, blue bar) average Rg mostly shows up within 2.18 to

2.2 nm whereas the native structure of the protein (Right panel, WP, orange bar) samples over a wide range of Rg values starting from 2.17 to 2.21 nm.

The RMSF depicts the flexibility at the residual level. From Fig. 18, we see that the fluctuation of the backbone C_α RMSD is bit higher for first 50 ns of the simulated trajectory hence we have divided the total production runtime into two equal halves to capture the time dependent characteristics of this time averaged data. As represented in Fig. 20, the pattern of flexibility is similar for WP and PL systems and is observed between 0.08 to 0.24 nm for both time intervals. While moving from the ‘0-50 ns’ time interval to the ‘50-100 ns’ time interval both plot shows greater stability signifies an overall decrease in fluctuation as simulation time progresses. We find that for both time intervals PL (blue curve) shows lesser residual fluctuation compared to the WP (orange curve) caused from restricted internal motion owing to the interaction with the ligand **LH_2**. Next, we focus on the fluctuation of the docked residue. In the left panel of Fig. 21 we place the systems next to each other for comparison purpose. We find that the docked site residues are more stable during the simulation, which is could be due to the recognition of the ligand by the ligand-binding region. In the right panel of Fig. 21 we represent the extent of stability of the docked residue by calculating ΔRMSF (%).It can be seen that stability of at least 10% is attained after docking in terms of residual fluctuation from the equilibrium position. A maximum stability of ~33% is observed for the ASP-295 while ASN-203 shows a

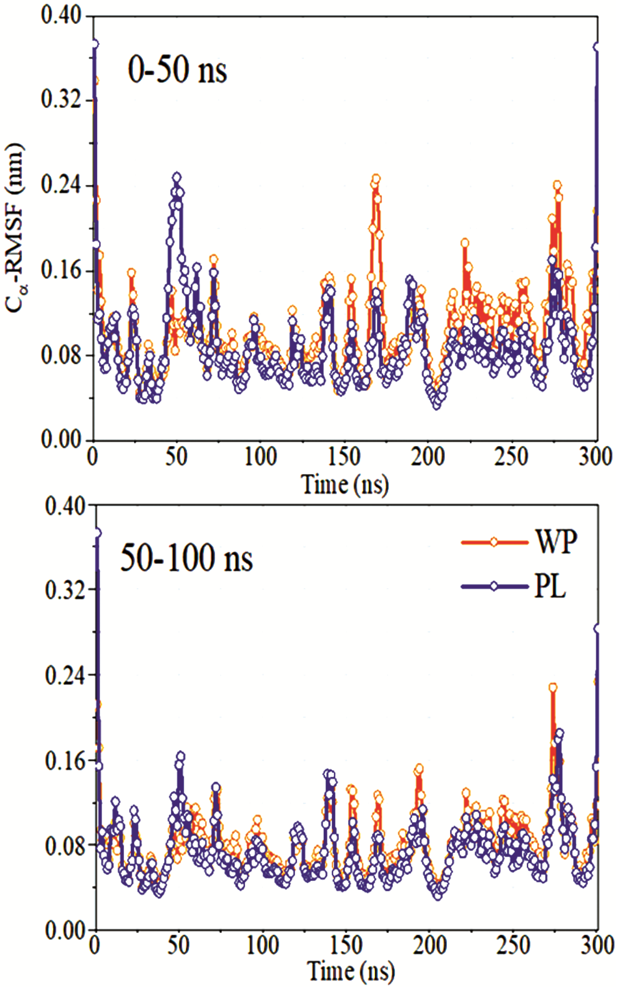

Fig. 20 — RMSF of the C_α atoms of 7O46 for two systems namely, WP (orange) and PL (blue). Left and right panel represent average RMSF value for 0-50 ns and 50-100 ns respectively

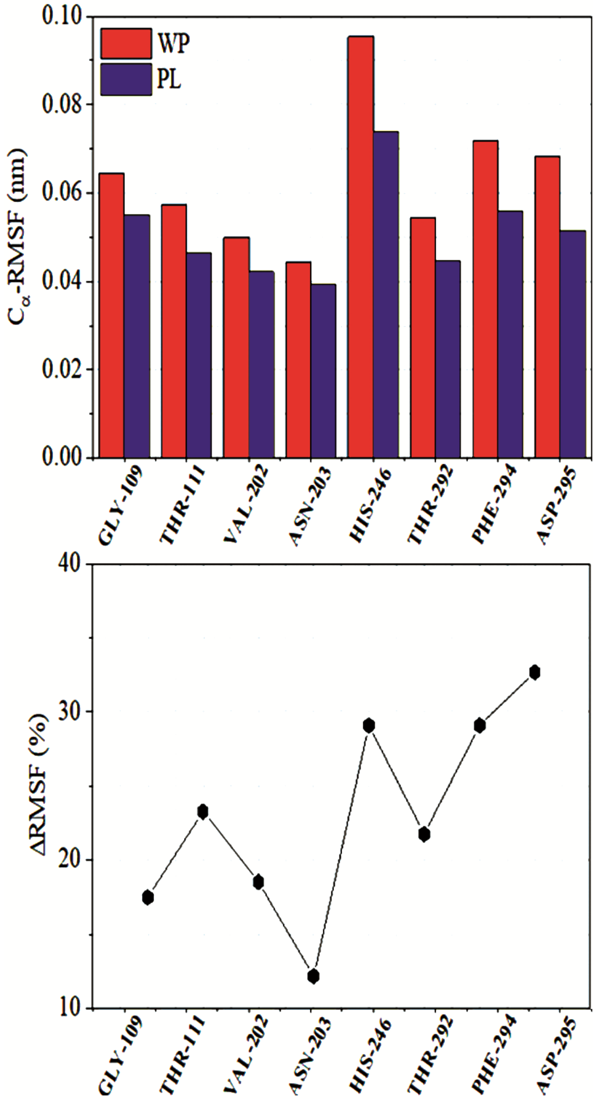

Fig. 21 — RMSF of the C_α atoms (left panel) and ΔRMSF (%) (right panel) of the docked residues calculated for two systems namely, WP (orange) and PL (blue)

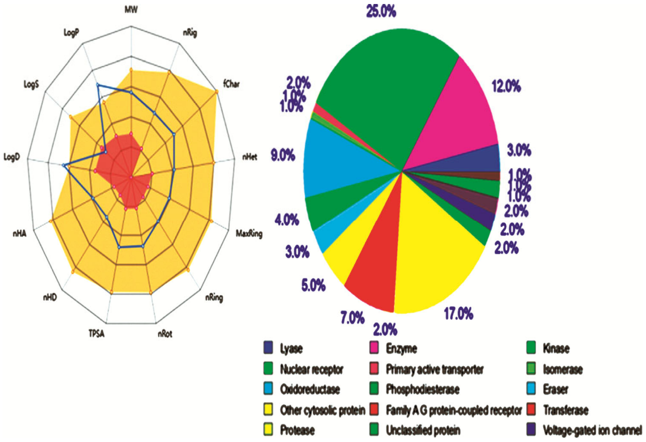

Fig. 22 — The graphical representation for salen-type compound $\mathbf{LH_2}$ with Swiss-target predictions

difference in fluctuation of ~12% on docking. These findings tell that the target protein is getting stabilized on binding with the chosen ligand (LH_2) docked against it. Thus the binding of the drug has significant impact on the residue fluctuation, and hence both correlated and non-correlated motions are affected.

Physiochemical and pharmacokinetic properties

A large variety of in silico methods share the objective of predicting ADME parameters from molecular structure and their pharmacokinetic and physicochemical parameters[38]. The potential theoretical biological activities of all the synthesized salen-type Schiff base compounds ($\mathbf{LH_2}$-$\mathbf{L^4H_2}$) were virtually designed *in silico* evaluation and the comparative results are summarized in the Table S3. These compounds attained all the drug likeness properties[39]. However, they are suitable for pharmacokinetics response. These complexes arepredicted not orally bioavailable, because too flexible and too polar structures. These compounds are also substrate or inhibitor of isoenzymes governing important pharmacokinetic behaviors and pharmacokinetics related drug-drug interactions. Fig. 22 shows the graphical representation for salen-type compound $\mathbf{LH_2}$ with Swiss-target predictions. The Swiss-ADME analysis results of the synthesized salen-type Schiff base compounds ($\mathbf{LH_2}$-$\mathbf{L^4H_2}$) are to be found comparatively higher than that of chloroquine (CQ) and Hydroxychloroquine (HCQ) as anti-SARS-CoV-2 drugs[26]. An integrated online platform for accurate and comprehensive predictions of ADMET properties. It has been widely recognized that absorption, distribution, metabolism, excretion and toxicity. Determines some physicochemical properties and medicinal chemistry friendliness. With significant updates to functional modules, predictive models, explanations, and the user interface, ADMET has greater capacity to assist medicinal chemists in accelerating the drug research and development process[40]. Table S4 show the physiochemical properties of synthesized salen type compounds ($\mathbf{LH_2}$-$\mathbf{L^4H_2}$) while Table S5 represents the pharmacokinetics properties of the investigated salen-type compounds ($\mathbf{LH_2}$-$\mathbf{L^4H_2}$). Fig. S31 and S32 shows the Swiss target and the bioavailability radar prediction, respectively for synthesized compounds ($\mathbf{L^1H_2}$-$\mathbf{L^2H_4}$). The physicochemical and pharmacokinetics results of synthesized compounds ($\mathbf{L^1H_2}$-$\mathbf{L^2H_4}$) are summarized as:

Pgp-substrate

Modulation of P-glycoprotein mediated transport has significant pharmacokinetic implications for Pgp substrates. The output value is the probability of being Pgp-substrate with the salen type compounds ($\mathbf{LH_2}$, $\mathbf{L^1H_2}$, $\mathbf{L^2H_2}$, $\mathbf{L^3H_2}$, $\mathbf{L^4H_2}$) are 0.003, 0.927, 0.004, 0.279, and 0.867.

HIA: Human intestinal absorption of an oral drug is the essential prerequisite for its apparent efficacy. Accordingly, molecules with a HIA >30% were classified as HIA- (Category 0), while molecules with a HIA < 30% were classified as HIA+ (Category 1). The output value is the probability of being HIA bearing with the salen type compounds ($\mathbf{LH_2}$, $\mathbf{L^1H_2}$, $\mathbf{L^2H_2}$, $\mathbf{L^3H_2}$, $\mathbf{L^4H_2}$) are 0.025, 0.002, 0.101, 0.005, and 0.02.

$\mathbf{F_{20\%}}$: The human oral bioavailability 20% which shows the indicator efficiency of the drug delivery to the systemic circulation. Molecules with a bioavailability ≥ 20% were classified as $F_{20\%}$-(Category 0), while molecules with a bioavailability < 20% were classified as $F_{20\%}$+ (Category 1). The output value of $\mathbf{F_{20\%}}$ containing salen type compounds ($\mathbf{LH_2}$, $\mathbf{L^1H_2}$, $\mathbf{L^2H_2}$, $\mathbf{L^3H_2}$, $\mathbf{L^4H_2}$) are 0.265, 0.265, 0.165, 0.201, 0.004.

$\mathbf{F_{30\%}}$: The human oral bioavailability 30% shows the indicator of the efficiency of the drug delivery to the systemic circulation. Molecules with a bioavailability ≥ 30% were classified as $F_{30\%-}$(Category 0), while molecules with a bioavailability < 30% were classified as $F_{30\%}$+ (Category 1). The output value is the probability of being $F_{30\%}$+, with the salen type compounds ($\mathbf{LH_2}$, $\mathbf{L^1H_2}$, $\mathbf{L^2H_2}$, $\mathbf{L^3H_2}$,

L^4H_2) are 0.031, 0.997, 0.01, 0.669, and 0.001, respectively.

Caco-2 Permeability

The human colon adenocarcinoma cell lines (Caco-2), as an alternative approach for the human intestinal epithelium, has been commonly used to estimate *in vivo* drug permeability due to their morphological and functional similarities. salen type compounds (**LH_2, L^1H_2, L^2H_2, L^3H_2, L^4H_2**) are considered to have a proper Cao-2 permeability if it has predicted value > -4.15log cm/s. The output value is the Caco-2 Permeabilitywith the salen type compounds (**LH_2, L^1H_2, L^2H_2, L^3H_2, L^4H_2**) are -5.164, -5.328, -5.360, -5.247 and -4.927, respectively.

PPB: Plasma protein binding of a drug to proteins in plasma has a strong influence on its pharmacodynamics behavior. PPB can directly influence the oral bioavailability because the free concentration of the drug is at stake when a drug binds to serum proteins in this process. A salen type compounds (**LH_2, L^1H_2, L^2H_2, L^3H_2, L^4H_2**) are considered to have a proper PPB if it has predicted value < 99%, and drugs with high protein-bound may have a low therapeutic index. The output value of PPB with the salen type compounds (**LH_2, L^1H_2, L^2H_2, L^3H_2, L^4H_2**) are 96.45, 100.6, 97.56, 98.52 and 98.39%, respectively.

VD (Volume Distribution): The VD is a theoretical concept that connects the administered dose with the actual initial concentration present in the circulation and it is an important parameter to describe the *in vivo* distribution for drugs. The unit of predicted VD is L/kg. A compound is considered to have a proper VD if it has predicted VD in the range of 0.04-20 L/kg. The output value of VD with the salen type compounds (**LH_2, L^1H_2, L^2H_2, L^3H_2, L^4H_2**) are 0.983, 0.696, 0.877, 0.629 and 1.367, respectively.

BBB Penetration

Drugs that act in the CNS need to cross the blood–brain barrier (BBB) to reach their molecular target. By contrast, for drugs with a peripheral target, little or no BBB penetration might be required in order to avoid CNS side effects. The unit of BBB penetration is cm/s. Molecules with logBB > -1 were classified as BBB+ (Category 1), while molecules with logBB ≤ -1 were classified as BBB- (Category 0). The output value is the probability of being BBB+, within the range of 0 to 1.

Fu: The fraction unbound in plasms. Most drugs in plasma will exist in equilibrium between either an unbound state or bound to serum proteins. Efficacy of a given drug may be affect by the degree to which it binds proteins within blood, as the more that is bound the less efficiently it can traverse cellular membranes or diffuse. Result interpretation: >20%: High Fu; 5-20%: medium Fu; <5% low Fu.

Substrate or inhibitor of isoenzymes

Based on the chemical nature of biotransformation, the process of drug metabolism reactions can be divided into two broad categories: phase I (oxidative reactions) and phase II (conjugative reactions). The human cytochrome P450 family (phase I enzymes) contains 57 isozymes and these isozymes metabolize approximately two-thirds of known drugs in human with 80% of this attribute to five substrate or inhibitor of isoenzymes (CYP1A2, CYP2C19, CYP2C9, CYP2D6, CYP3A4) governing important pharmacokinetic behaviors. Inhibitions of these isoenzymes are certainly one major cause of pharmacokinetics related drug-drug interactions. Most of these CYPs responsible for phase I reactions are concentrated in the liver. Result interpretation: Category 0: Non-substrate / Non-inhibitor; Category 1: substrate / inhibitor. The output value is the probability of being substrate / inhibitor, within the range of 0 to 1.

CL: The clearance of a drug. Clearance is an important pharmacokinetic parameter that defines, together with the volume of distribution, the half-life, and thus the frequency of dosing of a drug. The unit of predicted CL penetration is mL/min/kg. >15 mL/min/kg: high clearance; 5-15 mL/min/kg: moderate clearance; <5 mL/min/kg: low clearance.

T1/2:The half-life of a drug is a hybrid concept that involves clearance and volume of distribution, and it is arguably more appropriate to have reliable estimates of these two properties instead. Molecules with T1/2 > 3 were classified as T1/2 - (Category 0), while molecules with T1/2 ≤ 3 were classified as T1/2 + (Category 1). The output value is the probability of being T1/2+, within the range of 0 to 1.

hERG Blockers: The human ether-a-go-go related gene. The During cardiac depolarization and repolarization, a voltage-gated potassium channel encoded by hERG plays a major role in the regulation of the exchange of cardiac action potential and resting potential. The hERG blockade may cause long QT syndrome (LQTS), arrhythmia, and Torsade de Pointes (TdP), which lead to palpitations, fainting, or even sudden death. Molecules with IC_{50} more than 10 μM or less than 50% inhibition at 10 μM were classified as hERG - (Category 0), while molecules with IC_{50} less than 10 μM or more than 50% inhibition at 10 μM were classified as hERG+ (Category 1). The output value is the probability of being hERG+, within the range of 0 to 1.

H-HT: The human hepatotoxicity. Drug induced liver injury is of great concern for patient safety and a major cause for drug withdrawal from the market. Adverse hepatic effects in clinical trials often lead to a late and costly termination of drug development programs. Category 0: H-HT negative (-); Category 1: H-HT positive (+). The output value is the probability of being toxic, within the range of 0 to 1.

DILI: Drug-induced liver injury (DILI) has become the most common safety problem of drug withdrawal from the market over the past 50 years. Category 0: DILI negative (-); Category 1: DILI positive (+). The output value is the probability of being toxic, within the range of 0 to 1.

Eye Corrosion /Irritation: Assessing the eye irritation/corrosion (EI/EC) potential of a chemical is a necessary component of risk assessment. Cornea and conjunctiva tissues comprise the anterior surface of the eye, and hence cornea and conjunctiva tissues are directly exposed to the air and easily suffer injury by chemicals. There are several substances, such as chemicals used in manufacturing, agriculture and warfare, ocular pharmaceuticals, cosmetic products, and household products, which can cause EI or EC. Category 1: corrosives / irritants chemicals; Category 0: non-corrosives / non-irritants chemicals. The output value is the probability of being toxic, within the range of 0 to 1.

Respiratory Toxicity

Among these safety issues, respiratory toxicity has become the main cause of drug withdrawal. Drug-induced respiratory toxicity is usually under diagnosed because it may not have distinct early signs or symptoms in common medications and can occur with significant morbidity and mortality. Therefore, careful surveillance and treatment of respiratory toxicity is of great importance. Category 1: respiratory toxicants; Category 0: non-respiratory toxicants. The output value is the probability of being toxic, within the range of 0 to 1.

***I*GC_{50}**:48 hour Tetrahymena pyriformis IGC_{50} (concentration of the test chemical in water in mg/L that causes 50% growth inhibition to Tetrahymena pyriformis after 48 hours). The unit of IGC50 is −log10 [(mg/L)/(1000*MW)].

LC_{50}FM:96 hour fathead minnow LC_{50} (concentration of the test chemical in water in mg/L that causes 50% of fathead minnow to die after 96 hours). The unit of LC_{50}FM is −log10 [(mg/L)/(1000*MW)].

LC_{50}D: 48 hour Daphnia magna LC_{50} (concentration of the test chemical in water in mg/L that causes 50% of Daphnia magna to die after 48 hours). The unit of LC_{50}DM is −log10 [(mg/L)/(1000*MW)].

NR-AR-LBD: Androgen receptor (AR), a nuclear hormone receptor, plays a critical role in AR-dependent prostate cancer and other androgen related diseases. Endocrine disrupting chemicals (EDCs) and their interactions with steroid hormone receptors like AR may cause disruption of normal endocrine function as well as interfere with metabolic homeostasis, reproduction, developmental and behavioral functions. Category 1: actives; Category 0: inactive. Molecules that labeled 1 in this bioassay may bind to the LBD of androgen receptor. The output value is the probability of being actives, within the range of 0 to 1.

SR-MMP: Mitochondrial membrane potential (MMP), one of the parameters for mitochondrial function, is generated by mitochondrial electron transport chain that creates an electrochemical gradient by a series of redox reactions. This gradient drives the synthesis of ATP, a crucial molecule for various cellular processes. Measuring MMP in living cells is commonly used to assess the effect of chemicals on mitochondrial function; decreases in MMP can be detected using lipophilic cationic fluorescent dyes.

Experimental Section

Materials used for synthesis

The chemicals used were of AnalaR grade. 5-Bromosalicylaldehyde, 3,5-Dichlorosalicylaldehyde, 5-Bromo-3-methoxy-2-hydroxy-benzaldehyde, 3,5-Diiodosalicylaldehyde, 3,5-Dinitrosalicylaldehyde, ethylene diamine were obtained from Sigma-Aldrich and were used without further purification.

Instrumentation

^{1}H NMR, ^{13}C NMR, FT-IR and UV-Vis spectral techniques were recorded in order to confirm structural elucidation of the desired products. Elemental analytical data and quantum chemical calculations were also applied for these purposes. The FT-IR spectra of the compounds were recorded on a Shimadzu IR Affinity-1S Fourier trans- form infrared spectrophotometer in the range 4000-400 cm^{-1} range using KBr pellets and the electronic spectra of the compounds were taken on a Thermo-scientific UV-Vis recording spectrophotometer Evolution-3000 in quartz cells.Melting point was measured on a Boetius micro melting point apparatus. NMR spectra were recorded on a BrukerUltrashield 500 plus 500 MHz FT-NMR Spectrometer.

Single crystal X-ray diffraction

The structure of **LH$_2$**was determined by single crystal X-ray crystallography at 220(2) K using Bruker SMART APEXII CCD diffractometer, equipped with graphite-crystal incident beam monochromator, and a fine focus sealed tube with Mo-Kα (λ= 1.54178 Å). The Bruker SMART software and Bruker SAINT Software were used for data acquisition and data reduction, respectively. The structure was solved by direct methods and refined by full-matrix least-square calculations with the SHELXL-2018/3 software package[41]. All non-hydrogen atoms were refined anisotropically, and all hydrogen atoms on carbon were placed in calculated positions, guided by difference maps and refined isotropically. The molecular and crystal structure was plotted using ORTEP[42].

Quantum computational analysis

In computational chemistry, quantum mechanical methods are widely used for understanding the electronic properties, molecular orbital and molecular electrostatic properties. The electronic structure calculation of series of a new of salen-type Schiff base compounds (**LH$_2$-L^{4}H$_2$**) were carried out by the *Gaussian 16* package[43]. The cif file format of series of new salen-type Schiff base compounds (**LH$_2$-L^{4}H$_2$**) were used for geometrical optimization for the synthesized structure. The optimized structure, the lowest unoccupied molecular orbitals (LUMO), and the highest occupied molecular orbitals (HOMO), and 3D molecular electrostatic potential maps (MEPs) were computed and visualized using *Gaussview 5.0*[44]. For each of the salen-type Schiff base compounds (**LH$_2$-L^{4}H$_2$**), HOMO-LUMO energy gap, ionization potential (IP), electron affinity (EA), electro negativity (χ), chemical potential (μ), global hardness (η), global softness (σ) and global electrophilicity (ω), were calculated from the energies of the HOMO and LUMO as reported considering Parr and Pearson's interpretation of DFT and Koopmans theorem.

Molecular docking protocols

Molecular docking studies were carried out to analyze the binding energy of a series of new salen-type Schiff base compounds (**LH$_2$-L^{4}H$_2$**) for selected viral proteins of SARS-CoV-2 M^{pro} and HIV virus. The SARS-CoV-2 main protease was selected for molecular docking and X-ray crystallographic structure of SARS-CoV-2 M^{pro} was obtained from Protein data Bank[36] (PDB ID: 7O46; space group: C121; unit cell: a = 113.666 Å, b = 54.064 Å, c = 44.931 Å, α = 90°, β = 101.47 °, γ = 90°) and used as receptor protein. Similarly, the Human immunodeficiency virus type-1 bound to HIV-1 RNA was selected for molecular docking study. The X-ray crystallographic structure of the HIV-1 RNA virus (PDB ID: 1UUI) was retrieved from the protein data bank and used as receptor proteins[45]. The X-ray crystallographic structure of DNA polymerase IV PDB ID: 5YUX) was obtained from Protein data Bank[46] (space group: P1211; unit cell: a = 86.07 Å, b = 57.09 Å, c = 109.99 Å, α = 90°, β = 94.5 °, γ = 90°) and used as receptor protein. Initially, the protein coordinates were prepared by deleting all the water and heteroatoms to make the targeted protein receptor-free. Further, the polar hydrogens and Kollman charges were added to the protein using the *Autodock tool* (ADT) 1.5.6 associated with *Autodock 4.2*[47]. The prepared protein and ligand coordinates are saved in a.pdbqt file format using ADT software. The gird box of the desired volume is selected in such a way that the ligand can rotate freely inside the active site pocket protein. The configuration files are generated using the coordinates and dimension of the grid box. *Vina Lamarckian* genetic algorithm generates[48] the output files having predicted free energy for binding sites. The result comprises of different poses with corresponding energies were analyzed and high-quality figures are rendered by *Biovia Discovery Studio* 2020 [49].

Hirshfeld surface analysis

An intermolecular interaction of the **LH_2** ligand was analysed using Hirshfeld surfaces and fingerprint graphs. The molecular Hirshfeld surfaces (HSs) and their associated two-dimensional fingerprint plots (FPs) was generated for ligand **LH_2** based on their crystallographic information file (cif), using *CrystalExplorer 17.5* software[50]. The 3D graphical plots of the HSs are mapped over the d_{norm} (normalized contact distance) surface enables us to visualize the various intermolecular interactions in the crystal lattice and allows us to gain insight into the crystal packing behaviour. The HS is reduced to 2D fingerprint plots by obtaining standard resolution of molecular HS on calculating the *d*i and *d*e for each surface point. The *d*i and *d*e are the distance to the HSs from the nearest internal nucleus (inside the HSs) and external nucleus (outside the HSs), respectively. Furthermore, the energy framework analysis is carried out in order to explore the intermolecular interaction energies between the molecular pairs within the cluster of radii 3.8 Å. These calculations were performed using *Crystal Explorer 17.5* combined with CE-B3LYP/6-31G(d,p) functional/basis set. The radius of the cylinder connected to the centroids of the pairs of molecules represents the magnitude of interaction energies and relative strength of the molecular packing in a different direction. Using energy framework analysis supramolecular architecture of the crystal structure can be visualized[51].

Pharmacokinetic and drug-likeness prediction

The prediction of ADMET properties in drug development is important to research that helps to prevent drug failure during the clinical stages. For this reason, the best-identified salen-type Schiff base compounds (**LH_2-L^4H_2**) were evaluated using pkCSM[52] for their *in silico* pharmacokinetic parameters to avoid the failure of the ligands during clinical trials and to improve their chances of reaching the stage of potential candidate drugs. Its absorption in the human intestine; percolation of the blood–brain barrier and the central nervous system, and its metabolism indicate the chemical biotransformation of a drug by the body, total clearance of drugs and the toxicity levels of the molecules. The drug-likeliness of a molecule was expressed using Lipinski's rule of five parameters (molecular weight <500 Da, no more than 5 hydrogen bond donors, no more than 10 hydrogen bond acceptors and logP should not be greater than 5). Lipinski's rule of five properties was obtained from the SwissADME server (https://www.swissadme.ch/index.php).

Simulation Details

GROMAC[37] molecular dynamics package (version 2021.1) along with OPLS-AA force field[53] is used to model the protein and the ligand LH_2 and to define the existing interactions. The functional form of the FF is given in equation 1 which is as follows,

$$V = \sum_{bonds} K_r(r - r_{eq})^2 + \sum_{angles} K_\theta(\theta - \theta_{eq})^2 + \sum_{n=0}^{5} C_n(cos(\emptyset - 180°))^n + \sum_{i<j} \left(\frac{q_i q_j e^2}{r_{ij}} + 4\varepsilon_{ij}\left[\left(\frac{\sigma_{ij}}{r_{ij}}\right)^{12} - \left(\frac{\sigma_{ij}}{r_{ij}}\right)^{6}\right]\right) \quad \ldots (1)$$

Here, harmonic terms for the bond stretching (bond distance, r; bond distance at equilibrium, r_{eq}; bond force constant, K_r) and angle bending (bond angle, θ; bond angle at equilibrium, θ_{eq}; angle force constant, K_θ) is used to define the intramolecular bonded interactions. C_n represent the coefficients for the Ryckaert-Bellemans form of the proper dihedral potential and ϕ is defined as the dihedral angle. The non-bonded inter-actions consist of two terms namely, Lennard–Jones (LJ) and Coulomb interactions. We define the Lennard–Jones radii, potential well depth and the distance between the atoms as σ_{ij}, ε_{ij} and r_{ij}, respectively. Considering the Coulomb interactions, q_i and q_j are the respective partial charges. In this simulation, the geometric combination rules are used for the Lennard–Jones coefficients,

$$\sigma_{ij} = (\sigma_{ii}\sigma_{jj})^{1/2} \quad \varepsilon_{ij} = (\varepsilon_{ii}\varepsilon_{jj})^{1/2} \quad \ldots (2)$$

To model the water molecules, SPC/E potential[54] is considered in this study. The topological parameters for the protein are generated through the pdb2gmx tool of the GROMACS (version 2021.1). OPLS-AA force field compatible online automatic topology construction utility LIGPARGEN[55-57] is used to collect the bonded and non-bonded parameters for the ligand **LH_2**. To obtain a solvent relaxed initial configuration, a 5000-steps energy minimization is performed for each system (WP and PL) using the steepest decent algorithm[58]. Simulations are performed at RT *i.e.* 298 K, in order to avoid any temperature accelerated consequences and to solely probe the effect of the ligand on the protein moiety considered in this investigation. The equilibration process is divided into two steps. The first step involves a 500 ps run under the canonical (NVT) ensemble to heat each system from 0 K to 298 K and to get rid-off the void formation in the simulation box. The next step follows a 40 ns equilibration at the isothermal-isobaric (NPT) ensemble with a reference pressure of 1 Bar. This period of equilibration is sufficient enough to generate a well equilibrated system to start with. Temperature of the systems is kept constant by applying the *V*–rescale thermostat[59] whereas; Parrinello–Rahman barostat[60] with a pressure relaxation time of 2 ps is used for the attainment of the desired pressure. Production run for 100 ns with an integration time step of 2 fs is performed and the trajectory is saved at a frequency of 20 ps for analysis. During equilibration and final production run all bonds are kept constrained using the LINCS algorithm[61]. Short range Lennard–Jones interactions are accounted using the minimum image convention [62]. To estimate the non-bonded interactions including the electrostatic as well as van der Waals forces, a spherical cut-off of distance 1 nm is chosen. Periodic boundary condition is employed in all three dimensions for removing the edge effects. Long range electrostatic interactions are calculated using the particle mesh Ewald (PME) method[63]. VMD 1.9.3 [64] is used to visualize the trajectories and capture snapshots of the protein and ligands.Next, we report the root-mean-square deviation (RMSD), and radius of gyration (R_g) of C_α atoms of the protein backbone to check the stability and root-mean-square fluctuation (RMSF) for the residual flexibility considering the systems under investigation. The results for the systems are plotted together for the sake of comparison.

General synthesis procedure

Synthesis of 2,2'-((1E,1'E)-(ethane-1,2-diylbis(azaneylylidene)) bis(methaneylylidene)) bis(4-bromophenol), LH_2

A tetradentate-N_2O_2 Schiff base (**LH_2**) ligand was synthesized by the refluxing 5-Bromosalicylaldehyde (20.0 mmol, 4.02 g) with ethylenediamine (10.0 mmol, 0.54 mL) in 2:1 molar ratio in EtOH for 5 hrs. On cooling the solution to RT, green crystals suitable for single crystal X-ray diffraction were recovered from mother liquor, which were filtered, washed with MeOH and then washed with diethyl ether (5×5 mL). The crystals were then dried in air at RT, and store in a desiccator over $CaCl_2$. Yield 95%. m.p.>280°C. Anal. Calcd for $C_{16}H_{14}Br_2N_2O_2$: C, 45.10; H, 3.31; N, 6.57. Found: C, 45.11; H, 3.32; N, 6.58%. FAB-MS: *m/z* Obsd. (Calcd) 423.94 (423.96 g/mol.); ^1H NMR (500 MHz, $CDCl_3$): δ 13.12 (*s*, 1H, Ar-OH), δ 8.28 (*s*, 1H, -N=CH), δ 7.34 (*s*, 1H, Ar-H), δ 7.26(*d*, 1H, Ar-H), 6.85(*d*, 1H, Ar-H), δ 3.94 (*t*, 2H, $-CH_2$); ^{13}C NMR (500 MHz, $CDCl_3$): δ 165.34, 160.07, 135.18, 133.57, 119.93, 119.06, 110.20, 59.60; UV-Vis (MeOH): λ (nm): 265(π-π*) and 340 (n-π*); IR (KBr): 1641 (>C=N); 3440 (υAr-OH), 1474 (υAr-C-C), 636 cm^{-1} (υC-Br). Some representative spectral data (^1H NMR, ^{13}C NMR and FT-IR) of tetradentate salen-type ligands are given in the supporting information (Figure S1-S9).

Synthesis of 6,6'-((1E,1'E)-(ethane-1,2-diylbis(azaneylylidene))bis(methaneylylidene))bis(2,4-dichlorophenol),L^1H_2

L^1H_2 ligand was synthesized as brown crystalline product by the refluxing 3,5-Dichlorosalicylaldehyde (20.0 mmol, 3.82 g) with ethylenediamine (10.0 mmol, 0.54 mL) in 2:1 molar ratio in EtOH for 5 hrs. The brown transparent crystalline product was obtained, which was filtered, washed with diethyl ether and stored in a desiccator over $CaCl_2$. Salen-type ligand gave satisfactory elemental analysis. Yield 80%. m.p.>275°C. Anal. Calcd for $C_{16}H_{12}Cl_4N_2O_2$: C, 47.32; H, 2.98; N, 6.90. Found: C, 47.33; H, 2.99; N, 6.91%. FAB-MS: *m/z* Obsd. (Calcd) 403.97 (403.99 g/mol.); ^1H NMR (500 MHz, $CDCl_3$): δ 13.91 (*s*, 1H, Ar-OH), δ 8.28 (*s*, 1H, -N=CH), δ 7.40 (*s*, 1H, Ar-H), δ 7.26 (*d*, 1H, Ar-H), δ 7.14 (*d*, 1H, Ar-H), δ 4.01 (*t*, 2H,$-CH_2$); ^{13}C NMR (500 MHz, $CDCl_3$): δ 165.27, 156.11,132.49, 129.23, 123.11, 122.75, 119.40, 58.98; UV-Vis (MeOH): λ (nm): 275(π-π*) and 330 (n-π*); IR (KBr): 1634 (>C=N); 3051 (υAr-OH), 1493 (υAr-C-C), 845 cm^{-1} (υC-Cl).

Synthesis of 2-bromo-6-((E)-((2-(((E)-5-bromo-2-hydroxy-3-methoxybenzylidene)amino)ethyl)imino)methyl)-4-methoxy-phenol, L^2H_2

$L^2H_2$was synthesized in a similar manner as **L^1H_2**by the refluxing 5-Bromo-3-methoxy-2-hydroxy-benzaldehyde (20.0 mmol, 4.62 g) with ethylenediamine (10.0 mmol, 0.54 mL) in 2:1 molar ratio. The brown transparent crystalline product was obtained, which was filtered, washed with diethyl ether and stored in a desiccator over $CaCl_2$. Yield 70%. m.p.>277°C. Anal. Calcd for $C_{18}H_{18}Br_2N_2O_4$: C, 44.47; H, 3.73; N, 5.76. Found: C, 44.48; H, 3.74; N, 5.75%. FAB-MS: *m/z* Obsd. (Calcd) 483.96

(483.98 g/mol.); ^{1}H NMR (500 MHz, $CDCl_3$): δ 13.53 (*s*, 1H, Ar-OH), δ 8.24 (*s*, 1H, -N=CH), δ 7.26 (*s*, 1H, Ar-H), δ 6.99 (*d*, 1H,Ar-H), δ 3.96 (*s*, 3H, Ar-OCH_3), δ 3.85 (*t*, 2H,-CH_2); ^{13}C NMR (500 MHz, $CDCl_3$): δ 167.96, 165.67, 151.04, 149.40, 125.16, 125.09, 119.11, 117.37, 109.51, 59.29, 56.28; UV-Vis (MeOH): λ (nm): 270 (π-π*) and 325 (n-π*); IR (KBr): 1627 (>C=N); 3079 (υAr-OH), 2940 (υAr-OCH_3), 670 cm^{-1} (υC-Br).

Synthesis of 6,6'-((1E,1'E)-(ethane-1,2-diylbis (azaneyl ylidene))bis (methaneylylidene))bis(2,4-diiodophenol), L^3H_2

L^3H_2 was synthesized in a similar fashion **L^2H_2** by the refluxing 3,5-Diiodosalicylaldehyde (20.0 mmol, 7.46 g) with ethylenediamine (10.0 mmol, 0.54 mL) in 2:1 molar ratio. The yellow transparent crystalline product was obtained, which was filtered, washed with diethyl ether and stored in a desiccator over $CaCl_2$. Yield 72%. m.p.>250°C. Anal. Calcd for $C_{16}H_{12}I_4N_2O_2$: C, 24.90; H, 1.57; N, 3.63. Found: C, 24.91; H, 1.58; N, 3.64%. FAB-MS: *m/z* Obsd. (Calcd) 771.71 (771.75 g/mol.); ^{1}H NMR (500 MHz, $CDCl_3$): δ 12.52 (*s*, 1H, Ar-OH), δ 8.54 (*s*, 1H, -N=CH), δ 7.53 (*s*, 1H, Ar-H), δ 7.12 (*s*, 1H,Ar-H), δ 3.96 (*t*, 2H, -CH_2); ^{13}C NMR (500 MHz, $CDCl_3$): δ 162.54, 158.21, 146.68, 136.90, 118.16, 89.50, 58.23; UV-Vis (MeOH): λ (nm): 260 (π-π*) and 345 (n-π*); IR (KBr): 1648 (>C=N); 3410 (υAr-OH), 1485(υAr-C-C), 1250, 510 cm^{-1} (υC-I).

Synthesis of 6,6'-((1E,1'E)-(ethane-1,2-diylbis (azaneyly lidene))bis(methaneylylidene))bis(2,4-dinitrophenol), L^4H_2

L^4H_2 was synthesized in a similar manner as **L^3H_2** by the refluxing 3,5-dinitrosalicylaldehyde (20.0 mmol, 4.24 g) with ethylenediamine (10.0 mmol, 0.54 mL) in 2:1 molar ratio. The brown transparent crystalline product was obtained, which was filtered, washed with diethyl ether and stored in a desiccator over $CaCl_2$. Yield 84%. m.p.>272°C. Anal. Calcd for $C_{16}H_{12}N_6O_{10}$: C, 42.87; H, 2.70; N, 18.75. Found: C, 42.88; H, 2.71; N, 18.76%. FAB-MS: *m/z* Obsd. (Calcd) 448.06 (448.08 g/mol.); ^{1}H NMR (500 MHz, $CDCl_3$): δ 11.53 (*s*, 1H, Ar-OH), δ 8.65 (*s*, 1H, -N=CH), δ 8.10 (*s*, 1H, Ar-H), δ 7.92 (*s*, 1H,Ar-H), δ 4.12 (*t*, 2H, -CH_2); ^{13}C NMR (500 MHz, $CDCl_3$): δ 163.58, 156.13, 142.53, 135.26, 133.83, 131.62, 126.28, 68.23. UV-Vis (MeOH): λ (nm): 280 (π-π*) and 335 (n-π*); IR (KBr): 1645 (>C=N); 3415 (υAr-OH), 1525 (υAr-NO_2), 1475 cm^{-1} (υAr-C-C).

Conclusion

In conclusion, in this work we reported five new salen-type Schiff base compounds (**LH_2-L^4H_2**) were designed and synthesized, and their interaction with SARS-CoV-2 and HIV virus was studied by molecular docking methods for possible biomedical applications. Molecular docking studies were performed on salen-type Schiff base compounds (**LH_2-L^4H_2**) to predict the binding mode and interactions between the ligands and the main protease of the SARS-CoV-2 (PDB ID: 7O46) for COVID-19 and HIV virus (PDB ID: 1UUI). The molecular docking results showed that salen-type Schiff base compounds (**LH_2-L^4H_2**) may be used as anti-COVID-19(anti-SARS-CoV-2) and anti-HIV drugs. As potential drug candidates, Swiss-ADME and target predictions (pharmacokinetics and drug-likeness prediction) analyses are also studied and the results are compared with Chloroquine and Hydroxychloroquine as anti-SARS-CoV-2 drugs.

Acknowledgements

The authors are thankful to the Sophisticated Analytical Instrument Facility (SAIF), IIT Madras, India for single crystal data collection of **LH_2**. We must thanks to the Crystallographer, Shobhana Krishnaswamy, IIT Madras. One of the authors, SK is thankful to NIT Patna, India for providing research fellowship under TEQIP.

Author Contributions

Sunil Kumar: Formal analysis, Investigation, Software. Data Curation.Mukesh Choudhary: Supervision, Conceptualization, Methodology, Visualization, Writing-original draft, Resources.

Supplementary Information

Supplementary information is available in the website http://nopr.niscpr.res.in/handle/123456789/58776.

Optimized structure, HOMO-LUMO orbital energies, MEPs, Interaction energy diagrams, docked surface representation for Salen-type compounds are given in Supplementary Information.

Deposition number: CCDC- 2176825 for LH_2 contains the supplementary crystallographic data for this paper. This data can be obtained free of charge at www.ccdc.cam.ac.uk/conts/retrievel.html or www.ccdc.cam.ac.uk/structures or from the Cambridge Crystallographic Data Center, 12 Union Road, Cambridge CB2 1EZ, UK; fax: +44 1223/ 336 033. E-mail: deposit@ccdc.ac.uk.

References

1 (a) Venkataramanan N S, Kuppuraj G & Rajagopal S, *Coord Chem Rev*, 249 (2005) 1249; (b) Raihana H D, Karthick K,

Shankar T, Kamalesu S & Babu A A, *J Mol Struct*, 1264 (2022) 133217.

2 (a) Shukla S N, Gaur P, Raidas M L & Chaurasia B, *J Mol Struct*, 1202 (2020) 127362; (b) Yin H-Y, Tang J & Zhang J L, *Eur J Inorg Chem*, 2017 (2017) 5085; (c) Yang X, Jones R A, Rivers J H & Wohg W K, *Dalton Trans*, (2009) 10505, (https://doi.org/10.1039/B910588C).

3 Portakal E D, Kaya Y, Demirayak E, Yeldir E K, Ercag A, Kaya I, *J Coord Chem*, 75 (2022) 611.

4 Baleizao C & Garcia H, *Chem Rev*, 106 (2006) 3987.

5 Canali L, Sherrington D C, *Chem Soc Rev*, 28 (1999) 85.

6 Gurusamy S, Krishnaveni K, Sankarganesh M, Sathish V, Thanasekaran P & Mathavan A, *J Mol Liq*, 325 (2021) 115190.

7 Kumar S & Choudhary M, *J Biomol Struct* Dy, 2022, (https://doi.org/10.1080/07391102.2022.2076155).

8 Mohan B & Choudhary M, *J Mol Struct*, 1246 (2021) 131246.

9 Aprajita & Choudhary M, *J Mol Struct*, 1263 (2022) 133114.

10 GorbalenyaA E, Baker S C, Baric R S, Groot R J D, Drosten C, Galyaeva A A, Haagmans B L, Lauber C, Leontovich A M, Neuman B W, Penzar D, Perlman S, Poon L L M, Samborskiy D V, Sidorov I A, Sola I & Ziebuhr J, *Nat Microbiol*, 5 (2020) 536.

11 Sang P, Tian S H, Meng Z H & Yang L Q, *RSC Adv*, 10 (2020) 15775.

12 Zhang L, Lin D, Sun X, Curth U, Drosten C, Sauerhering L, Becker S, Rox K & Hilgenfeld R, *Science*, 368 (2020) 409.

13 Zang S, Krumberger M, Morris M A, Parrocha C M T, Kreutzer A G & Nowick J S, *Eur J Med Chem*, 218 (2021) 113390.

14 Zhang L, Lin D, Kusov Y, Nian Y, Ma Q, Wang J, Brunn A V, Leyssen P, Lanko K, Neyts J, Wilde A D, Snijder E J, Liu H & Hilgenfeld R, *J Med Chem*, 63 (2020) 4562.

15 Kumar S & Choudhary M, *New J Chem*, 46 (2022) 4911.

16 Kumar S & Choudhary M, *New J Chem*, 46 (2022) 7128.

17 Hosen M A, Munia N S, Al-Ghorbani M, Baashen M, Almalki F A, Hadda T B, Ali F, Mahmud S, Saleh M A, Laaroussi H & Kawsar S M A, *Bioorg. Chem*, 125 (2022) 105850.

18 Spackman M A & McKinnon J J, *Cryst Eng Comm*, 4 (2002) 378.

19 Spackman M A & Jayatilata D, *Cryst Eng Comm*, 11 (2009) 19.

20 Kumar S & Choudhary M, *Mol Crys Liq Crys*, 744 (2022) 45.

21 Frisch M J, Trucks G W, Schlegel H B, Scuseria G E, Robb M A, Cheeseman J R, Scalmani G, Barone V, Mennucci B, Petersson G A, Gaussian 16 Rev. A.03. Wallingford, CT, **2016**.

22 Lambert H, Mohan N & Lee T C, *Phys Chem Chem Phys*, 21 (2019) 14521; Seeberger P H & Werz D B, *Nature*, 446 (2007) 1046.

23 Koopmans T, *Physica*, 1 (1934) 104.

24 Wiederstein M & Sippl M J, *Nucleic Acids Res*, 35 (2007) W407.

25 Banti C, Kourkoumelis N, Hatzidimitriou A, Antoniadou I, Dimou A, Rallis M, Hoffmonn A, Schmidtke M, McGuire K, Busath D, Kolocouris A & Hadjikakou S K, *Polyhedron*, 185 (2020) 114590.

26 Ali A, Sepay N, Afzal M, Sepay N S, Alarifi A, Shahid M & Ahmad M, *Bioorg Chem*, 110 (2021) 104772.

27 Pal M, Musib D & Roy M, *New J Chem*, 45 (2021) 1924.

28 Hashim K K M, Manoj E & Kurup M R P, *J Mol Struct*, 1246 (2021) 131125.

29 Mizuhara A, Oishi S, Ohno H, Shimura K, Matsuoka M & Fujii N, *Org Biomol Chem*, 10 (2012) 6792.

30 Sun I C, Wang H K, Kashiwada Y, Shen J K, Cosentino L M, Chen C H, Yang L M & Lee K H, *J Med Chem*, 41 (1998) 4648.

31 Qian K, Yu D, Chen C H, Huang L, Natschke S L M, Nitz T J, Salzwedel K, Reddick M, Allaway G P & Lee K H, *J Med Chem*, 52 (2009) 3248.

32 (a) Scala A, Piperno A, Micale N, Christ F & Debysen Z, *ACS Med Chem Lett*, 10 (2019) 398; (b) Zhang Q, Su L, Collins J, Chen G, Wallis R, Mitchell D A, Haddleton D M & Becer C R, *J Am Chem Soc*, 136 (2014) 4325.

33 (a) Wang Q, Li Y, Zheng L, Huang X, Wang Y, Chen C H, Cheng Y Y, Natschke S L M, Lee K H, *ACS Med Chem Lett*, 11 (2020) 2290; (b) Jing B, Janout V, Herold B C, Klotman M E, Heald T, Regen S L, *J Am Chem Soc*, 126 (2004) 15930; (c) Wu T, Froeyen M, Kempeneers V, Pannecouque C, Wang J, Busson R, Clercq E D & Herdewijn P, *J Am Chem Soc*, 127 (2005) 5056; (d) Mishra L, Jha A, Itokawa H, Takeya K, *Indian J Chem*, 37A (1998) 747.

34 Baskaran S, Krishnan M M, Arumugham M N, Kumar R, *J Mol Struct*, 1224 (2021) 129236.

35 Atlam F M, El-Nahass M N, Bakr E A, Fayed T A, *Appl Organomet Chem*, *32* (2018) e3951.

36 Luttens A, Gullberg H, Abdurakhmanov E, Vo D D, Akaberi D, Talibov V O, Nekhotiaeva N, Vangeel L, Jonghe S D, Jochmans D, Krambrich J, Tas A, Lundgren B, Gravenfors Y, Craig A J, Atilaw Y, Sandstorm A, Moodie L W K, Lundkvist A, Hemert M J V, Neyts J, Lennerstrand J, Kihlberg J, Sandberg K, Danielson U H & Carlsson J, *J Am Chem Soc*, 144 (2022) 2905.

37 Hess B, Kutzner C, Spoel D V D & Lindahl E, *J Chem Theory Comput*, 4 (2008) 435.

38 Lipinski C A, *Drug Discov Today Technol*, 1 (2004) 337.

39 Mohan B, Choudhary M, Kumar G, Muhammad S, Das N, Singh K, Al-Sehemi A G & Kumar S, *Synth Comm*, 50 (2020) 2199.

40 Watanabe R, Esaki T, Ohashi R, Kuroda M, Kawashima H, Komura H, Kitatani Y N, Mizuguchi K, *J Med Chem*, 64 (2021) 2725.

41 Sheldrick G M, *Acta Crystallogr*, C 71 (2015) 3.

42 Farrugia L J, *J Appl Crystallogr*, 45 (2012) 849.

43 Chai J D & Gordon M H, *Phys Chem Chem Phys*, 10 (2008) 6615.

44 Lee C, Yang W & Parr R G, *Phys Rev* B, 37 (1988) 785.

45 Davis B, Afshar M, Varani G, Murchie A I H, Karn J, Lentzen G, Drysdale M J, Bower J, Potter A J & Aboul-Ela F, *J Mol Biol*, 336 (2004) 343.

46 Kottur J & Nair D T, *Nucleic Acids Res*, 46 (2018) 5875.

47 Park H, Lee J & Lee S, *Proteins*, 65 (2006) 549.

48 Seeliger D & Groot B L D, *J Comput Aided Mol*, 24 (2010) 417.

49 Systèmes D, BIOVIA, Discovery Studio Visualizer, Release 2019, *San Diego: Dassault Systèmes* 2020.

50 Tirado-Rives J & Jorgensen W L, *J Chem Theory Comput*, 4 (2008) 297.

51 Yang Y, Weaver M N & Merz K M, *J Phys Chem A*, 113 (2009) 9843.

52 Hosen M A, Munia N S, Al-Ghorbani M, Baashen M, Almalki F A, Hadda T B, Ali F, Mahmud S, Saleh M A, Laaroussi H & Kawsar S M A, *Bioorg Chem*, 125 (2022) 105850.
53 Kahn K & Bruice T C, *J Comput Chem*, 23 (2002) 977.
54 Mark P & Nilsson L, *J Phys Chem A*, 105 (2001) 9954.
55 Jorgensen W L & Tirado-Rives J, *Proc Nat Acad Sci USA*, 102 (2005) 6665.
56 Dodda L S, Vilseck J Z, Tirado-Rives J & Jorgensen W L, *J Phys Chem B*, 121 (2017) 3864.
57 Dodda L S, Vaca I C D, Tirado-Rives J & Jorgensen W L, *Nucleic Acids Res*, 45 (2017) 331.
58 Petrova S S & Solev'ev A D, *Hist Math*, 24 (1997) 361.
59 Bussi G, Donadio D & Parrinello M, *J Chem Phys*, 126 (2007) 014101.
60 Parrinello M & Rahman A, *J Appl Phys*, 52 (1981) 7182.
61 Hess B, Bekker H, Berendsen H J C & Fraaije J G E M, *J Comput Chem*, 18 (1998) 1463.
62 Allen M P & Tildesley D J, *Computer Simulation of Liquid*, (Oxford University Press, Clarendon, U K) 1987.
63 Darden T, York D & Pedersen L, *J Chem Phys*, 98 (1993) 10089.
64 Humphrey W, Dalke A & Schulten K, *J Mol Graphics*, 14 (1996) 33.